UNIVERSITY OF CALABRIA –Ph.D. School "Scienze e Ingegneria dell'Ambiente, delle Costruzioni e dell'Energia"

UNIVERSITY OF QUÉBEC – "Institut National de la Recherche Scientifique, Centre Énergie, Matériaux et Télécommunications"

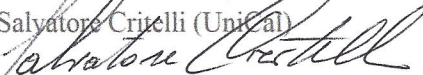**Dual degree joint Philosophiae Doctor (Ph.D.) program**

Cycle XXIX

Decoration and Characterization of Carbon-based nanomaterial for third generation photovoltaic devices

SSD: FIS/07

Coordinator: Prof. Salvatore Critelli (UniCal)
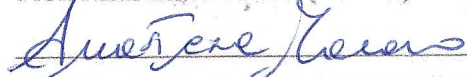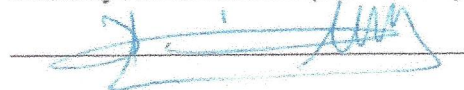
Supervisor/Tutor: Prof. Assunta Bonanno (UniCal)

Prof. Anastasia Macario (UniCal)

Prof. My Alì El Khakani (INRS-EMT)

Ph.D. student: Dott. Alessandra Imbrogno

University of Calabria

University of Québec - Institut National de la Recherche Scientifique Énergie, Matériaux et Télécommunications

---

Philosophiae Doctor (Ph.D) Thesis

Decoration and characterization of carbon-based nanomaterial for third generation photovoltaic devices

Supervisors:
Prof. Assunta Bonanno
Prof. My Ali El Khakani
Prof. Anastasia Macario

Ph.D Student:
Dr. Alessandra Imbrogno

SSD: FIS/07 - Academic year 2016/2017

Contents

Estratto

Il presente progetto di dottorato è orientato sulla sintesi e la caratterizzazione di nanomateriali a base di carbonio e sulla loro decorazione mediante la tecnica della deposizione con laser pulsato (Pulsed laser deposition – PLD), allo scopo di sviluppare nanomateriali avanzati adatti alle applicazioni fotovoltaiche, con particolare riguardo per il loro utilizzo all'interno di dispositivi "Dye-Sensitized Solar Cell" (DSSC). Le celle solari "dye-sensitized" appartengono alla terza generazione dei dispositivi fotovoltaici, e consistono principalmente di due elettrodi depositati su vetrini conduttivi FTO: il fotoanodo è anche detto "working electrode" (WE), è composto da un film sottile di biossido di titanio TiO_2 depositato sul vetro conduttivo FTO e sensitizzato da un colorante organico (dye), mentre il catodo, chiamato "controelettrodo" (CE), e formato da un film sottile di platino depositato via sputtering su un vetro conduttivo FTO. Lo spazio tra questi due elettrodi è riempito con una soluzione elettrolitica composta da una coppia redox. I principali vantaggi di queste celle solari rispetto a quelle tradizionali basate sul silicio sono la relativa facilità del processo di fabbricazione e l'uso di materiali che sono abbondanti sulla Terra. Tuttavia, l'efficienza della conversione della luce solare in energia elettrica è ancora insoddisfacente, con efficienze di conversione che a malapena raggiungono il 18% per le tipologie di DSSC a stato solido e del 10% per le DSSC a stato liquido. I principali problemi che affliggono l'efficienza delle DSSC sono la deteriorazione del colorante, l'alto tasso di ricombinazione elettrone-lacuna all'interno del film di TiO_2, le resistenze di contatto tra controelettrodo (CE) e soluzione elettrolitica, e la degradazione del controelettrodo di platino provocata dalla soluzione elettrolitica stessa. Nelle ultime due decadi, molti sforzi sono stati volti alla risoluzione di tali problemi e alcuni miglioramenti sono stati ottenuti grazie alla modifica di entrambi gli elettrodi. Questo progetto di dottorato è focalizzato sul miglioramento dei materiali utilizzati sia nel fotoanodo che nel catodo delle DSSC di tipo liquido mediante l'uso di nanomateriali a base di carbonio. In particolare per quanto riguarda il controelettrodo, si è sostituito il costosissimo platino con nanotubi di carbonio a pareti multiple (multi walled carbon-nanotubes - MWCNT) decorati tramite la tecnica della PLD con nanoparticelle metalliche che assicurano sia una buona resistenza all'azione corrosiva della soluzione elettrolitica, sia un'alta rugosità della

superficie che migliora la catalisi della reazione redox e comporta quindi un miglioramento delle performances del dispositivo DSSC. Per quanto riguarda il fotoanodo (WE), invece, questo progetto di dottorato è stato focalizzato sull'inserimento, all'interno del film di biossido di titanio TiO_2, di diversi nanomateriali a base di carbonio quali i nanotubi di carbonio a parete multipla e il grafene con lo scopo di ridurre la perdita di elettroni dovuta alla ricombinazione elettrone-lacuna. Anche in questo caso, i risultati mostrano interessanti miglioramenti dell'efficienza fotovoltaica del dispositivo DSSC. Tutti gli esperimenti sono stati condotti sia presso l'università degli Studi della Calabria (UniCal, Italia) sia presso l'Institut National de la Recherche Scientifique (INRS, Canada) nell'ambito degli accordi di cotutela del progetto di dottorato tra le due istituzioni scientifiche.

Abstract

The PhD project is oriented on the synthesis and characterization of carbon-based nanomaterial and their eventual decoration with pulsed laser deposition technique for the developing of advanced nanomaterial suitable for photovoltaic application, in particular in DSSC devices. The dye sensitized solar cells belong to the third generation of photovoltaic devices, and are mainly composed of two electrodes deposited on FTO conductive glasses: the photoanode is also called "working electrode" (WE) and it is made of a thin film of TiO_2 deposited on a conductive FTO glass and sensitized by an organic dye, while the cathode, called "counter electrode" (CE), is made of a thin film of platinum sputtered on a conductive FTO glass. The space between these two electrodes is filled with an electrolyte solution composed of a redox couple. The great advantage of these solar devices respect to traditional silicon-based solar devices is the relatively easy fabrication processes and the use of materials that are abundant on Earth. However, their conversion efficiency is still unsatisfactory, with conversion efficiency that barely reach the 18% for the solid-type DSSC and the 10% for the liquid-type of DSSC. The main issues that affect the photovoltaic efficiency in DSSC are the dye deterioration, the high e-/h+ recombination in TiO_2-dye substrate, the contact resistance between CE and electrolyte, and the degradation of the platinum counter electrode due to the electrolyte solution. During the last two decades many efforts have been made to resolve these issues, and some advances have been made by modify both the working and the counter electrodes. This Ph.D. project is focused on improving the materials used in both electrodes in liquid-type DSSC by using carbon nanomaterials. In particular, for what concern the counter electrode, the expensive platinum was substituted with multi walled carbon-nanotubes (MWCNT) decorated with metal nanoparticles that ensured both a good resistance to the corrosive action of the electrolyte solution and a highly rough surface that improved the catalysis of the redox reaction, resulting in a improvement of the photovoltaic performance of the DSSC device. For what concern the working electrode, instead, this Ph.D project was focused on the insertion of different carbon-based nanomaterials as multiwalled carbon nanotubes and graphene inside the TiO_2 thin film to reduce the loss of electron due to the e-/h+ recombination. Even in this case, the results showed interesting improvements

of the photovoltaic efficiency of the DSSC device. All the experiments were conducted in both University of Calabria (Italy) and Institut National de la Recherche Scientifique (Canada).

Abstrait

Le projet de thèse est orienté sur la synthèse et la caractérisation de nanomatériaux à base de carbone et leur éventuelle décoration par technique de dépôt laser pulsé pour le développement de nanomatériaux avancés adaptés à l'application photovoltaïque, en particulier dans les dispositifs DSSC. Les cellules solaires à colorant appartiennent à la troisième génération de dispositifs photovoltaïques, et sont principalement composées de deux électrodes déposées sur des verres conducteurs FTO: la photoanode est également appelée "électrode de travail" (WE) et est constituée d'un film mince de TiO_2 déposé sur un verre FTO conducteur et sensibilisé par un colorant organique, tandis que la cathode, appelée "contre-électrode" (CE), est constituée d'un film mince de platine pulvérisé sur un verre FTO conducteur. L'espace entre ces deux électrodes est rempli d'une solution d'électrolyte composée d'un couple redox. Le grand avantage de ces dispositifs solaires par rapport aux dispositifs solaires à base de silicium traditionnels réside dans les processus de fabrication relativement aisés et l'utilisation de matériaux abondants sur Terre. Cependant, leur efficacité de conversion est encore insatisfaisante, avec une efficacité de conversion atteignant à peine les 18% pour le DSSC de type solide et les 10% pour le DSSC de type liquide. Les principaux problèmes affectant l'efficacité photovoltaïque du DSSC sont la détérioration du colorant, la forte recombinaison e / h + dans le substrat TiO_2, la résistance de contact entre CE et l'électrolyte et la dégradation du contre-électrode en platine due à la solution d'électrolyte. Au cours des deux dernières décennies, de nombreux efforts ont été déployés pour résoudre ces problèmes, et certains progrès ont été faites en modifiant à la fois les électrodes de travail et les contre-électrodes. Ce projet de doctorat se focalise sur l'amélioration des matériaux utilisés dans les deux électrodes dans le DSSC de type liquide en utilisant des nanomatériaux de carbone. En particulier, pour ce qui concerne la contre-électrode, le platine onéreux a été remplacé par des nanotubes de carbone multi-parois (MWCNT) décorés de nanoparticules métalliques assurant à la fois une bonne résistance à l'action corrosive de la solution électrolytique et une surface fortement rugueuse qui améliore la catalyse de la réaction redox, résultant en une amélioration de la performance photovoltaïque du dispositif DSSC. Pour ce qui concernent la électrode de travail, ce projet de thèse s'est concentré sur l'insertion des

différents nanomatériaux à base de carbone comme les nanotubes de carbone à parois multiples et graphène pour réduire la perte d'électrons en raison de l'e- / h + recombinaison dans le substrat TiO_2. Même dans ce cas, les résultats ont montré des améliorations intéressantes de l'efficacité photovoltaïque du dispositif DSSC. Toutes les expériences ont été menées à la fois à l'Université de Calabre (Italie) et à l'Institut National de la Recherche Scientifique (Canada).

Introduction

The increase of pollution and environmental disaster due to the use of fossil combustibles has attracted the interest of scientific community, focusing the research on the develop of more suitable and "green" alternatives to satisfy the increase of energy demand without affecting negatively the environment.

The European Union, in particular, has been one of the major supporter in the development of more sustainable and ecological solution to meet with the constant increase of the energy demand. Since 2007, the EU strongly supported the exploiting of renewable energy sources inside the countries of the union, aiming to increase the production of renewable energy by a 20% by the end of 2020 [1].

The traditional silicon-based solar cell devices are still the most widely used photovoltaic technology, but their diffusion on larger scales is still limited by the high cost of production and of maintenance of these devices [2].

The development of more efficient solar panels and the optimization of the production processes, in order to decrease the costs of production, are the greatest challenges for the photovoltaic research field nowadays. The scientific community has experienced the growth of new alternative photovoltaic technologies in parallel with the implementation of the silicon-based devices. In particular, the research was focused on the development of new photovoltaic devices based on semiconductor materials that are greatly abundant on Earth, with the aim of substituting the expensive silicon with materials that allow to lower the cost of production without affecting, or even enhancing, the performance of the photovoltaic devices.

Traditionally, the photovoltaic devices are divided in three generations

- the first generation consists of silicon-based solar cells (mono or poly-crystalline silicon wafer) with efficiency that ranges from 12% to 17%. The main disadvantage of these solar cells is the high cost of production and the complex fabrication processes.

- the second generation includes thin film silicon-based solar cells. These devices use a thin film of amorphous silicon that replaces the expensive mono or polycrystalline wafer used in the first generation devices. Though the use of amorphous silicon has cheaper costs of production

with respect to the first generation photovoltaic devices, their efficiency reaches values of about 6%-10%, which are lower if compared to the traditional solar cells.

- the third generation of photovoltaic devices gathers all the alternative technologies that replaces silicon with other less expensive nanomaterials. Multi-juncion solar cells [3], dye-sensitized solar cells [4], organic solar cells [5] and hybrid organic-inorganic solar cells [6] are all included in this particular category. Among them, the DSSCs [7] are the most promising devices for a large scale production since they ensure low cost of production, but their development is currently limited by the low efficiency reached.

This Ph.D. project is focused on the improvement of the DSSC devices, with particular regard to the enhancement of their photovoltaic efficiencies in order to make a step further toward their large scale usage. This work is devoted to contribute in particular to the improvements of the materials used in both the photoanode and the cathode of the DSSC. This goal will be achieved by replacing the expensive platinum used in the cathode with cheaper nanomaterials and by decorating them by using a novel and easy approach. Also the photoanode will be modified with the introduction of different carbon-based materials in the TiO_2 layer in order to solve some of the problems that affect the performance of these solar cells devices and enhancing their photovoltaic efficiency.

Chapter 1

State of Art

1.1 Dye sensitized solar cells

The dye sensitized solar cells (DSSCs) were developed for the first time in 1991 by Graetzel and differ from the other photovoltaic devices for the easy fabrication processes and the relatively low cost of the used materials[7].

In Graetzel's cell, a thin film of TiO_2 sensitized with an organic dye is used as photoanode (or working electrode, WE) while the cathode (or counter electrode, CE) consists of a thin film of sputtered platinum. The space in between the electrodes is filled with a red-ox couple electrolyte solution (usually iodide/triiodide). Due to the presence of the organic dye as sensitizer, the Graetzel cell is also called "dye sensitized solar cell".

The working mechanism of a DSSC device is relatively simple and expects to mimics the natural process of photosynthesis: the incident light coming from the sun promotes some of the electrons of a particular dye molecule from the highest occupied molecular orbital (HOMO) to the lowest unoccupied molecular orbital (LUMO). The energy levels of LUMO in the dye molecules are very closer to the conduction band of the TiO_2 thin film, favouring the decay of the photo-excited electrons in the TiO_2 energy band. The photo-excited electrons decayed in the TiO_2 thin film cause a cascade production of electrons, and hence of holes, in the semiconductor, and participate in the charge transport from the working electrode (WE) to the counter electrode (CE). The electrons coming from the working electrode are collected on the counter electrode, where the presence of platinum as a catalyst favours the transfer of these electrons to the electrolyte solution [8, 9, 10, 11],thus enhancing the red-ox reaction that enables the dye molecules regeneration.

Despite the DSSCs have attracted a great attention due to the possibility to produce solar cells with a relatively low cost of production, their conversion efficiency is still unsatisfactory. The different processes taking place inside the solar cell are responsible for this low efficiency. These unfavourable processes include dye deterioration, electron/hole (e-/h+) recombination in

9

TiO$_2$-dye substrate, contact resistance between the CE and the electrolyte solution, degradation of the platinum counter electrode due to the electrolyte solution [12] and its high cost as a precious metal [13]. In order to improve the DSSCs performance, many efforts have been devoted to the improvement of the materials for both the CE and the WE.

1.2 Advances in the improvement of the counter electrode

For what concerns the counter electrode, the studies were mainly focused on the substitution of the expensive platinum with more affordable materials still maintaining the high catalytic activity of the electrode. The carbon-based nanomaterials were extensively investigated due to their good conductive properties [9, 10, 11], and their superior durability in time compared with the standard Pt-based counter electrode [14]. Moreover, they exhibit good catalytic properties [15]. Specifically, carbon nanotubes (CNT) are particularly effective thanks to their excellent conductivity properties [16, 17, 18] and their particular topology that ensures both a large number of active sites for the catalysis and a decrease of charge-transport resistance between the electrolyte and the counter electrode.

Nam et al. [18] used the well-aligned carbon nanotubes as a catalytic material instead of platinum for the counter electrode, and achieved a power conversion efficiency 10% greater with respect to the standard DSSCs using platinum at the CE. Koo et al. [14], instead, studied the resistance to corrosion of CNT and the stability over time of the DSSCs, comparing the results obtained for the CNT-based CE with those of the standard Pt-based CE. Surprisingly, the CNT-based counter electrode remained stable over five days, and its characteristic impedance remained unchanged. The Pt counter electrode was affected by corrosion due to the electrolyte solution that caused a loss of adhesion between the Pt itself and the FTO glass substrate. This loss caused then an increase up to three times of the series resistance over time during the five days of analysis.

Further studies on the CNT evidenced also that the high surface area and the presence of defects on their surface decrease the charge-transport resistance at the interface between the CNT CE and the electrolyte solution. This allows to enhance the electron transfer and the chemical reactivity of this material [19, 20, 21]. Another important parameter that positively influences the catalysis of the redox reaction is the diameter of the CNTs. The study conducted by Hwang et al. [21] on CNTs with various diameters, evidenced an improvement in the reaction rate and a lower interfacial reaction resistance for the CEs made with CNTs with large diameters.

All these beneficial effects can be further improved by decorating the CNTs with metal nanoparticles [22, 23, 24, 25, 26, 27], enhancing the pho-

voltaic performances of the DSSC with respect to both the standard Pt-based CE and the pristine CNT one. For example, Lin et al. [25] used the electrophoresis to deposit oxidized MWCNT on FTO substrates, and the electrodeposition to decorate them with CoS nanoparticles. The decorated CE showed an efficiency of about 6.96%, while the pristine CNT one achieved only a 2.91% efficiency, and the platinum one 5.91%.

Zheng et al. [23] improved the photovoltaic performance of the DSSC by encapsulating FeNi alloy nanoparticles directly *in situ* within the CNTs by using $[Ni_2Fe(CN)_6]$ as a precursor for the calcination process, that was conducted at 600°C in argon atmosphere. Their novel Pod(N)-FeNi counter electrode showed an efficiency of 8.82%, that was higher than the efficiency of both the pristine MWCNT CE (4.87%) and the Pt one (8.01%).

The explanation of these improvements of efficiency can be found in a change in the work function value of the carbon-based material due to the presence of the metal nanoparticles on its surface. The decoration with metal nanoparticles in fact allows to obtain work function values closer to the work function of the FTO glass [28], thus enhancing the electron transfer from the CE to the electrolyte solution.

Nowadays, there are many different chemical and physical techniques that can be successfully used to synthetize and deposit the metal nanoparticles on various carbon-based materials, such as carbon fibres [29, 30], carbon nanotubes [23, 25, 26], and recently graphene [31, 32]. Among all these techniques, the hydrothermal methods [30, 31, 32, 33, 34] is the most largely used, while other commonly used techniques are: calcination [27], electrode-position [25], electrospun method [29] and pyrolysis [23]. Unfortunately, all these techniques require chemical precursors to synthetize the nanoparticles, the processes are usually performed at high temperatures and need several hours to complete the chemical reaction. Moreover post-treatments with acids must be done in order to remove eventual residues. Most of these chemical precursors and post-treatment acids are extremely toxic and polluting, and both the high temperature and the long time of reactions have a severe economic impact on the production of these CEs. The development of alternative techniques for the synthesis and deposition of these metal nanoparticles is a prerogative. These new techniques could ensure an easy fabrication process coupled with a low impact on the environment. These are important features, in order to move toward the prospective of a mass production of these photovoltaic devices in the near future.

1.3   Advances in the improvement of the working electrode

For what concerns the working electrode, the research is focused on the addition of conductive materials in the TiO$_2$ thin film with the aim of

improving the transport of the photo-generated electrons from the film itself to the FTO substrate. Among all the possible materials, even in this case the carbon-based nanomaterials seem to be the most promising candidates to quench the electron-hole recombination phenomenon inside the TiO_2 film. In fact, several studies evidenced that the addition of carbon-based nanomaterials improves both the optical properties [35, 36, 37, 38, 39, 40] and the electrical properties [41] of the photoanode.

Moreover, several theoretical and experimental studies pointed out that doping TiO_2 with carbon is useful to drastically reduce the band gap of TiO_2 [35, 36, 37, 38, 42]. One of the problems that affect the DSSCs efficiency, as described before, is that the TiO_2 maximum of light absorption is centred in the UV region of the solar spectrum. The addition of carbon nanotubes in the TiO_2 film has been demonstrated to reduce the luminescence emission [39] and to increase of about 6% the absorbance in the visible region with respect to the pure TiO_2 photoanode [39, 40, 43].

Although the doping of TiO_2 is beneficial in enhancing the photovoltaic properties of the DSSC, it has been demonstrated that this doping is effective only for low MWCNT concentration. For concentrations that exceed the 1 wt.% of CNT with respect to the TiO_2, it was observed a quench of about 13% of the efficiency of the device if compared with the standard DSSC [44]. The reason of this dependence of the properties of the WE to the amount of carbon-based material used is due to a change in the sample's morphology. For example, for low MWCNT concentration the carbon nanotubes are well dispersed between the TiO_2 aggregates, "filling" the interstices between the TiO_2 grains and allowing to obtain a uniform MWCNT-TiO_2 film. For MWCNT concentrations > 5% the photoanodes appear as a bulk of CNTs with randomly positioned TiO_2 aggregates. The amount of carbon-based material used affects differently the optical properties and the dye absorption properties of the photoanode. For what concerns the optical properties, Barberio et al. [45] reported that the MWCNT-TiO_2 photoanodes showed a wide absorption signal in the visible region which is strictly dependent to the amount of carbon nanotubes used and goes from the 10% of pure TiO_2 to the 97% of 50 wt.% MWCNT-TiO_2 photoanode. For low MWCNT concentration (ranging between 0.2%-2%), the absorbance in the visible region increases from 60% to 80%, indicating that even with very low amounts of MWCNT it is possible to obtain a great improvement of the light absorption in the visible region. However, even if the optical properties greatly improve with the increase of MWCNT amount, it was observed that the excess of CNT causes a competitive phenomenon against the the charge transport inside the TiO_2 film, acting as a trap for the charges [41].

Among the carbon-based material, also the graphene is worth to be mentioned as a promising dopant material for the WE. Some recent studies pointed out that adding graphene to the TiO_2 film it is possible to enhance the photovoltaic performance of the DSSC device [46, 47, 48, 49, 50, 51, 52].

The graphene peculiar 2D structure allows it to disperse well among the TiO$_2$ grains, thus enhancing the collection of electrons and limiting the losses due to the electron/hole recombination phenomenon taking place inside the TiO$_2$ film. However, as already observed for the CNTs, also in this case an excess of this material negatively affects the photovoltaic performance of the DSSC device. This could be addressed to the formation of graphene aggregates that behave as electron/hole recombination centres, thus preventing charge transport through the TiO$_2$ thin film [48]. Another cause could be a competitive light harvesting against the dye molecules [47], although this interplay is still unclear. Some studies report that the addition of graphene to the TiO$_2$ film does not influence the dye absorption in the TiO$_2$ [52], while other state the exact opposite, asserting that the increase in the amount of absorbed dye by the TiO$_2$ film is due to the presence of graphene [49, 50, 51].

It is clear, then, that further investigation on the interaction of both MWCNT and graphene with the TiO$_2$ is necessary in order to better understand the major mechanisms influencing light absorption process and the consequent charge transfer in the MWCNT-TiO$_2$ and G-TiO$_2$ composites.

1.4 Objectives

This PhD project is oriented toward the synthesis and characterization of carbon-based nanomaterials and their decoration by Ni or CoNi nanoparticles by means of pulsed laser deposition (PLD) technique for the development of high performance DSSC devices. The main objectives of this Ph.D. project are the following:

Objective no.1: Improvement of the DSSC performance by enhancing the counter electrode (CE):

- to replace Pt with carbon nanotubes (CNTs) covered with Ni or Co-Ni nanoparticles. The CNTs will be deposited via the spray coating technique whereas the PLD will be used for the Co-Ni nanoparticless deposition. The aim is to calibrate the deposited Ni or CoNi nanoparticles dimensions and spatial distribution in order to enhance the CEs electron-transfer properties and the electrocatalytic activity.

- To use the Atomic Force Microscopy (AFM) and photovoltaic characterization of the novel Ni and CoNi nanoparticles/CNTs CEs, in order to investigate the possible relationship between the CEs surface morphology and their power conversion efficiency.

Objective no.2: Improvement of the DSSC performance by enhancing the working electrode (WE):

- to improve photocharge transport by reducing the electron-hole recombination phenomenon. This will be investigated by modifying the TiO$_2$

thin film with carbon-based materials such as graphene (G) or CNTs and investigate the dye absorption properties of the WE as well as its Power Conversion Efficiency (PCE).

Chapter 2

Methodology

2.1 Pulsed Laser Deposition (PLD)

The Pulsed Laser Deposition (PLD) is a laser-based deposition technique, in which the laser beam is focused on a metal target placed in a vacuum chamber in controlled atmosphere. The working principle is relatively simple and can be divided in three phases (or regimes):

- a first phase in which the laser beam is sent on the target surface, with a consequent production of heat and photo-ionization of the irradiated area that entails the evaporation of a thin layer of material from the target's surface;

- a second phase in which the incident laser beam interacts with the evaporated material, with an isothermal formation of plasma (the so-called "plasma plume", a cloud made of ions, atoms, molecules, electrons and small aggregates of particles);

- a third phase in which the plasma plume expandsward to the surrounding gas background along the normal direction with respect to the target surface. Thus, these ablated species are deposited on the substrate placed parallel to the target, forming a thin film. The thickness of the film depends on several parameters, such as the distance between target and substrate, the energy density of the laser beam, the number of laser ablation pulses (N_{LP}), and the background gas pressure.

The laser used for the PLD deposition is a KrF excimer laser (GSI Lumonics PM-844, $\lambda = 248$ nm, pulse duration of 14 ns, repetition rate of 20 Hz) and the ablation was conducted under a controlled background of 300mTorr of helium, while the target-substrate distance was set at 5.5 cm. Both the target and the sample holders were kept in rotation during the PLD deposition in order to ensure a uniform deposition on the substrate.

2.2   Atomic Force Microscopy (AFM)

The Atomic Force Microscopy (AFM) is a scanning-probe microscopy technique developed by Binning, Quate and Gerber in 1986, and it is largely applied in several research and industrial fields [53, 54]. The AFM is a non-destructive technique for the study of surface morphology at very high resolution. One of the peculiarity of this technique is the possibility to obtain 3D imaging of the surface. The surface is scanned using a sharp tip made of silicon or silicon nitride placed at the end of a small bar (cantilever) of about 100-400 µm length and of known elastic constant. The tip length is around few microns, and has a curvature that is generally below 10 nm. The sensibility of cantilever to forces ranging between 10-7 and 10-12 N allows to measure the breaking forces of singular chemical bonds. The tip size is important to acquire the real features of the surface and to ensure an atomic resolution. Thanks to the advances made in the piezoelectric transducers (PZT) is now possible to use the scanning probe microscopy (SPM) techniques to probe the surfaces with precisions below the Armstrong. The piezoelectric support, indeed, enables the movement of the cantilever along both z axis maintaining a constant force, and on the xy plane to analyse the sample surface. During the analysis, the cantilever is subjected to Van der Waals forces that are established between the tip and the sample. These forces determine special deflections and oscillation of the cantilever, whose amplitude can be measured through the reflection of a laser spot from the end of the cantilever to a PSDP detector constituted by a photo-diodes matrix capable to collect the (x, y) coordinates of the signal in each point. These signals are then elaborated in a 3D image by the computer connected to the AFM, providing information on the sample surface morphology. During the scan at fixed height, a feedback mechanism avoids the tip to break or get dirty on the sample surface. This feedback mechanism regulates the distance between the tip and the sample, keeping a constant force between them. The main operation methods are three:

- Contact mode, in which the force between the tip and the sample is kept at a constant value by controlling the cantilever deflection.

- Non-contact mode, in which the cantilever oscillates at frequencies that are close to resonance. The Van der Waal forces between the tip and the sample surface provoke some variation in the oscillation that can be compared with the external reference oscillation to obtain useful information on the sample characteristics. This analysis mode has the disadvantage that the tip must be kept at a very close distance to the surface in order to be able to evaluate the deflections. Therefore, there is a possibility that the tip may stuck on the surface.

- Dynamic mode, in which the cantilever oscillates and enter in contact

with the surface at each cycle, allowing to measure the force necessary
to separate the tip from the sample.

Both non-contact mode and dynamic mode include the modulation in both
frequency and amplitude. In the former mode, the variation of the oscillation
frequency provides information about the sample surface characteristic. The
latter mode instead is also called "tapping mode": the variation of the
oscillation amplitude provides information about the surface topography
of the sample. Moreover, the phase variation generated when operating in
tapping mode can be used to identify the different types of materials present
on the surface. Compared with other microscopy techniques, such as SEM
and TEM, the AFM technique has the advantage of provide a 3D image
of the real analysed surface, and the sample does not need pre-treatments
before the analysis. Moreover, the AFM analysis can be conducted in air or
in liquid and it is not necessary to work in UHV conditions while it is for
both the SEM and the TEM techniques. The main disadvantage of AFM
respect to the electronic microscopy techniques is that the image dimension
has a maximum height in the order of micrometre and a maximum area of
about 100 µm x 100 µm while the SEM has both image area and depth of
field in the order of millimetre. Another disadvantage of AFM technique
is that images take a long time to be acquired. Indeed, the scansion of a
selected area of the sample requires several minutes while a SEM analysis
permits to scan an area in real time but with a relatively low quality [55].
The instrument used in this Ph.D. project is an AFM microscope (Icon
Bruker) working in "tapping mode"; the images have a resolution of 512
x 512 lines and were acquired with a scanning velocity of 0.5 Hz. All the
obtained images were elaborated using Nanoscope software (provided by
Bruker) in order to evaluate the roughness of the surface.

Power Spectral density

The Power Spectral density (PSD) is a useful tool to analyse the roughness
of surfaces. This function, in fact, represents the amplitude of the roughness
of the surface as a function of the roughness' spatial frequency. The spatial
frequency is defined as the inverse of the wavelength of the roughness char-
acteristics.
The PSD function, then, reveals the periodic surface characteristics that
would otherwise appear as random feature, and provides a graphical repre-
sentation of the features distribution.
This kind of surface analysis is useful for the determination of any noise
source, fibrous grains and other material characteristics. Moreover, the PSD
can be used to determine the atomic periodicity or crystalline lattice if used
at high magnification [56].

PSD and surface characteristic

The synthetic surface represented in fig.2.1 is mainly composed of two dominant wave forms, one with a long period along the x axis and another one with a short period along the y axis.
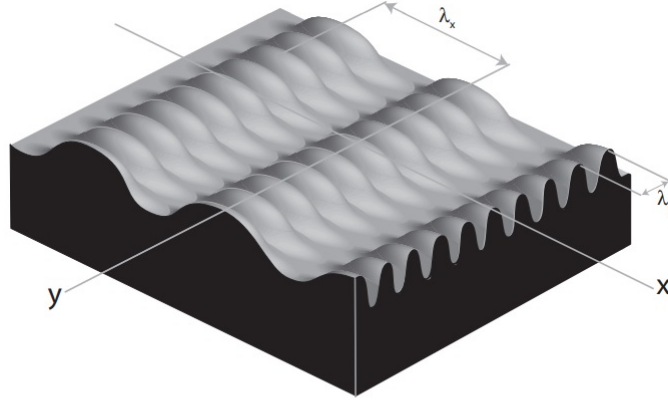
Figure 2.1: Waveform surfaces [56]

The 2D PSD of this surface consists of two dominant peaks (each correspond to one of the two main wavelengths), and of a number of smaller peaks related to eventual fine structures and/or border conditions.

Thanks to the sinusoidal waveform of this composite, the whole surface can be described by using just a small set of spectral frequencies. In the case of images containing angular waveforms, instead, more spatial frequency components are needed to describe the composite's surface [56].

PSD algorithm

Over a certain spatial frequencies range, the total power of surface is equal to square RMS roughness of the sample. The frequency distribution for a computerized profile of length L constituted of N points at d_0 intervals can be approximated as in the following:

$$PSD(f) = \frac{2d_0}{N} \left| \sum_{n=1}^{N} z(n) e^{i\frac{2\pi}{N}(n-1)(m-1)} \right|^2 \qquad \text{per: } f = \frac{m-1}{Nd_0}$$

where the f frequencies goes from $\frac{1}{L}$ to $\frac{(N/2)}{L}$ and i is the imaginary unit. For practical purpose, the algorithm used to calculate the PSD depends on

the square FFT of the image to obtain the power.
After the power P has been calculated, it can be used to calculate several values similar to PSD:

$$1DPSD = \frac{P}{\Delta f}$$

$$1DisotropicPSD = \frac{P}{2\pi f}$$

$$2DisotropicPSD = \frac{P}{2\pi f(\Delta f)}$$

The terms used at denominator are obtained from a progressive sampling of data from the 2D FFT from the image centre (as visually explained in fig.2.2).
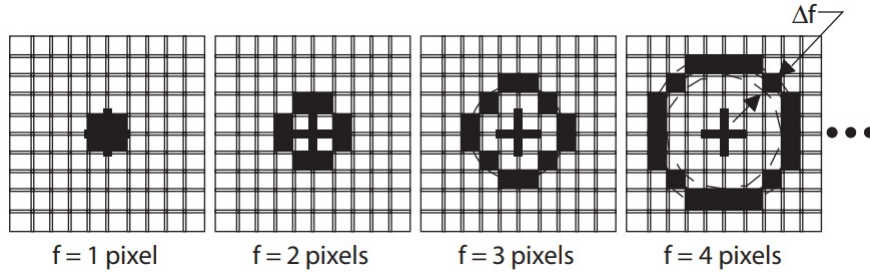

Figure 2.2: progressive data sampling [56]

Each sampling swings a data bucket of a certain frequency f, and since the samples are taken form the image centre, the sampling frequency f is limited to $\frac{(N/2)}{L}$ where N is the dimension in pixel of the scanned area. It also represents the upper bandwidth limit (that is the maximum frequency or the Nyquist frequency) of PSD graph, while the lower limit is defined at $\frac{1}{L}$ [56].

2.3 Scanning Electron Microscopy microscopy (SEM)

The Scanning Electron Microscopy (SEM) is an electro-optical instrument that uses a focused primary electrons beam instead of a photon beam to create images of the sample. The primary electron beam scans point by

point and line by line the sample inside a small rectangular area. During the interaction between the primary electron beam and the atoms of the samples the emission of electrons and X−rays occurs, including the secondary electrons that are collected by a detector and converted in electrical signals that are sent to the monitor in real time, where a similar scansion takes place at the same time. The result is a high resolution b/w image with high depth of field. Compared with traditional microscopy techniques, the high depth of field of SEM permits to obtain images with a characteristic 3D appearance which is very useful to understand the surface structure of the investigated sample. Moreover, its high resolution allows to obtain a greater magnification of fine details. Another great advantage of this technique is the use of electromagnets instead of lens. This ensures a strict control on the magnification of the image.
SEM apparatus is showed in fig. 2.3.

Figure 2.3: SEM apparatus used during the experimental activity

It consists of an electron gun with an electron source (usually a tungsten filament); a controller electrode constituted of a perforated cylinder called "Wehnelt" which allows to focus the emitted electrons in the so-called cross-over region where the source image is formed; a perforated circular electrode called anode that, by means of a variable bias voltage in the range 0-50 kV accelerates the electrons. Subsequently, an electromagnetic lens system creates a smaller crossover image on the sample plane. The beam diameter may have a value ranging from few nanometers to few tens of nanometers. Finally a diaphragm regulates the angular aperture of beam on the sample. During its path the beam is deflected by a series of electromagnetic fields generated from the scan system, that allows to cover the sample surface with a sequence of parallel and equidistant lines.
The primary electrons beam interacts with the sample, generating several effects as the emission of secondary electrons and the back-scattering of

electrons, but it is also possible that the primary electrons beam give energy to the electron of the atoms of the sample, causing the emission of UV, IR and X-Ray from the sample. This emitted radiation can be collected by some detectors and displayed on a screen. An amplifier increases the level of the collected signal, allowing the contrast increase, the differentiation, the integration and other forms of image manipulation usually used to evidence the high frequency and low intensities components that follow the detected band and can contain further information. Moreover, during the analysis the sample can be moved along the x, y and z axis, and can be turned and tilted in several directions [53].
In this thesis, the SEM characterization was conducted using a FEI / PHILIPS MOD. QUANTA 200F microscope, while the X-Ray microanalysis (EDX)was performed using— an Electron Microprobe Analyser (EMPA) – JEOL JXA 8230

2.4 Chemical characterization

2.4.1 Thermogravimetric Analysis (TGA)

The thermogravimetric analysis (TGA) is an experimental technique commonly used to measure the mass of the sample as a function of sample temperature or as a function of time. The measure can be performed in different ways: keeping the sample at a constant temperature (isothermal measurements), heating the sample at a constant heat rate (dynamic measurements) or subjecting it to a non-linear temperature program (sample controlled measurements, or SCTGA). The TGA measurements generate a graph of the mass (or per cent mass) as a function of the temperature and/or the time. Sometimes it is useful to also generate the first derivative of the TGA curve (called differential thermogravimetric, DTG) that evidences the mass change rate. The mass variation is due loss or gain of mass, and these variations appear as steps on the TG curve. The mass variation could be due to different factors:

- loss of water;

- evaporation of volatile components from the sample;

- oxidative decomposition of organic compounds or oxidation of metals, in air or oxygen atmosphere;

- pyrolysis or carbonization of organic compounds in inert atmosphere;

- decarboxylation or condensation reactions.

The change in the temperature during the TGA measurements determines a change in the gas density. This buoyancy effect can be corrected by subtracting a blank curve (or baseline, obtained by performing a blank measurement without the sample) from the TGA curve of the sample. Some instruments subtract a standard baseline from all measurements. The TGA measurement could be influenced by several factors, such as:

- the parameters used;

- the sample preparation;

- the crucible used;

- buoyancy and gas flow effects;

- changes in the sample physical properties due to the heating process;

- movements of the sample during the measurement.

Some of them, such as the buoyancy effects or the sample movements can be corrected or prevented.

The quantitative TGA evaluation involves the determination of step height. Sometimes, the first derivative curve can be a useful tool to easily individuate the correct temperature range in which the loss of mass takes place: on the DTG curve, in fact, a well evident peak represents the mass loss. The sum of all the steps plus the residuals is equal to the initial mass of the sample (100%). The loss quantification is performed using a horizontal evaluation, measuring the mass change before and after the mass loss. If the compound completely disappears during the measurement, it is easier to determine the mass loss. In this case, in fact, the percentage content can be evaluated as:

$$G[\%] = \frac{\Delta m}{m_0} \times 100\% \qquad (2.1)$$

where Δm is the mass loss and m_0 is the initial mass. In case of partial mass loss (as in stoichiometric reaction i. e. decarboxylation or dehydration), G can be calculated as:

$$G(\%) = \frac{\Delta m}{m_0} \times \frac{M}{nM_{gas}} \times 100\% \qquad (2.2)$$

where M is the original molar mass and M_{gas} is the eliminated gases molar mass and n is the number of moles of gas eliminated during the reaction for each mole of sample.

The TGA analyser used during the experiment is a by NETZCH instrument, operating under an airflow of 50 cc/min and with a heating rate of 5 °C/min.

2.4.2   X-Ray Photoelectron spectroscopy

Chemical characterization of all materials used during this PhD project was conducted using X-Ray Photoelectron spectroscopy (XPS).

The experimenta set-up is composed by a X-ray source, an analyser and an ultra-high vacuum (UHV) chamber.

The sample to be analysed was mounted on a precision manipulator (descibed in the following paragraphs) inside the UHV chamber and its surface chemical composition was evaluated using the XPS technique.

UHV system

The measurements was conducted in UHV in order to avoid sample contamination from atmospheric gases. The optimal measurements conditions are obtained when the pressure inside the chamber is at least $10^{-8} - 10^{-11}$ Torr. For this reason, the measurement takes place in a sealed environment constituted of the UHV chamber, which is made of steel and is equipped with several instruments and a pump system. The pump system is composed of three pumps that have three different working principles. The contemporary presence of three different pumps is fundamental, in order to achieve the low pressure necessary for the XPS measurement.

The first pumping stage uses a mechanical rotary dry pump that works without oils. This device works by means of an electrical engine that allows the rotation of two palettes inside a cylindrical cavity, which compress the gas coming from the chamber towards the exhaust valve. By using this first pumping stage it is possible to obtain a low vacuum level inside the chamber, with a pressure of around 10^{-3} Torr. This is because as the pressure inside the chamber reaches a certain value, the compressed gas is no more able to open the exhaustion valve. The second pumping stage uses a turbomolecular pump, a device which consists of a wide entrance with a rotor connected to a system composed of various palettes mounted on to several disks, forming several alternate layers. The distance between the layers is around 1 mm. When the rotation speed is high (around 60000 rpm), each layer gives a high momentum to the gas until it reaches the next layer, creating a pressure difference between the pump entrance and the exit.

The high operating speed of rotor hinders the use of this pump stage at atmospheric pressure, because the gas viscosity at atmospheric pressure is too high and can cause the distortion of the palettes. The second pumping stage allows to achieve a middle level of vacuum inside the chamber, with pressures in the $10^{-6} - 10^{-8}$ Torr range. It is impossible to go beyond these pressure values using a turbomolecular pump, because the remaining gases inside the chamber are composed of very light elements as hydrogen. These gases can be pumped out of the chamber using a third pumping stage.

The third pumping stage is composed of an ionic pump, that has a very

different working principles compare with the previous two systems. The first and the second pumping stage, in fact, are connected to each other in series, so that the gases expelled from the turbomolecular pump are injected in the rotary pump. The third stage works in parallel with the two previous stages. The ionic pump is a trapping device composed of a sealed steel parallelepiped box. In the upper side of the box there is a wide entrance that allows to directly connect the pump to the chamber.

Inside of the box, there are two titanium electrodes having a high potential varying from 3 to 7 kV. These electrodes consists of groups of several star-shaped cells in order to maximize the lateral surface of the entire group. The aim of this particular geometry is to maximize the surface of each electrode, in order to obtain a high pumping capacity. When the gas is in between the two titanium electrodes, it is ionized by a permanent magnet placed on the external side of the pump. The cathode collects the positive charges while the anode collects the negative ones. As the ions hit the cathode, they remove some titanium atoms; some of them will fall on the cathode surface, trapping the ion while the remaining ones will fall on the anode, creating a thin metallic layer able to chemical adsorb gases coming from the chamber (chemical pumping).

The cathode tends to be contaminated by the presence of ions coming from the ionized gas and, as a consequence, it decreases its pumping capacity. In order to solve this problem it is necessary to regenerate or replace the electrodes. The regeneration process occours by means of an incandescent titanium filament that emits atoms via sublimation process. The titanium emitted from the filament is deposited on both electrodes, covering all the impurities accumulated on the electrodes. Using the ion pump, the internal pressure inside the UHV chamber reaches a value of about 10^{-10} Torr [57]. The next step is the degassing stage, which takes place by heating the chamber using electrical resistors. The temperature reached during this stage is tipically around 100°C - 120°C. The operation usually lasts for two days, based upon the internal pressure of the chamber. After the degassing process, it is possible to reach pressure values around 10^{-10} Torr. The pressure inside the chamber is measured using two pressure sensors, placed in two different zones of the chamber. These sensors work in a pressure range from atmospheric pressure (760 Torr) to 10^{-10} Torr and the two sensors are linked together at a pressure value of 10^{-4} [58, 59]. A collimation system selects and focuses the electrons. It is possible to vary the electron beam energy and in addition, the electron beam can be deflected on a orthogonal plane respect to the beam direction. The sample to be investigated via XPS spectroscopy is mounted on a rigid stand that can be rotated with respect to the symmetry axes of the UHV chamber, and allows also small movements along the x, y, and z axes. The movements can be done using a manipulator placed on the external side of the chamber.

Vacuum gauge

The vacuum gauge used in this PhD project is composed of a filament supplied with current and a grid with a ion collector placed on its centre. The electrons are produced via thermionic effect by the filament, and they are accelerated toward the grid which is posed to a positive potential; the electrons impact on other molecules,causing their ionization. These ions are accelerated toward the collector. From the ionic current measured on the collector is possible to obtain the pressure, using an appropriate calibration.

Electrostatic analyser

The electrostatic analyser permits to measure the energy of a charged particle. It is composed of two metallic semi-spheres with a potential difference between them that allows only the charges with a specific value E of energy to reach the other terminal of the analyser by giving them a suitable curvature. The condition is:

$$\Delta V = V \left(\frac{R_2}{R_1} - \frac{R_1}{R_2} \right) \qquad \text{where: } E = qV$$

This energy is called pass-energy. Immediately after the terminal exit is placed a channeltron, constituted of a glass tube covered with a high resistive material, so that as the electrons hit its walls, it causes the emission of other electrons. Subsequently, these electron are accelerate causing, therefore, a cascade mechanism. For each electron that enters the channeltron, other 104 are generated. The so produced current will be then transformed in a series of pulses whose frequency is proportional to the initial current intensity. The analyser has two different working modes:

$$\Delta E = cost \qquad \text{and} \qquad \frac{\Delta E}{E} = cost$$

In the first mode, tension between the two semi-spheres is constant and the charges that arrives to the analyser are accelerated or decelerated by a lens system at the entrance. As result, their energy reach the same value of pass-energy, guaranteeing a ΔE constant resolution. In the second mode, the pass-energy is variable and the electrons are analysed at their energy; moreover, ΔE increases together with the energy, and the relative resolution $\frac{\Delta E}{E}$ is constant. The analyser is mounted on a goniometer inside the chamber and can be rotated. This allows to collect the electrons emitted from the sample at different angles, with an angular acceptance of about 2 degrees.

Data acquisition system

The data are acquired by means of a computer with Keithley KPCI-3108 interface for the analogic-digital and digital-analogic conversions. By means

of this interface, it is possible to select the tension to apply to the lens of the analyser, setting the energy for the analysis and receiving the related signals. The final data are averaged on several acquisitions, in order to reduce the noise effects.

XPS

X-ray Photoelectron Spectroscopy is based on the analysis of the energy of electrons emitted by a condensed matter as a consequence of its interaction with the electromagnetic radiation having energy in the x-ray range. X-rays are used during the photoionization process and possess energy that can penetrate relatively deep inside the sample, reaching a depth in the order of μm). Nevertheless, the emitted photoelectrons are subjected to intense inelastic scattering processes inside the atomic matrix with an energy loss that prevents their emission from the sample. Only electrons emitted from surface atoms (i.e. at a maximum depth of 10 to 20 atomic layers) are subjected to low amounts of collisions and can escape from the sample surface, thus giving their contribute to the signal detected by the analyser. The electrons that are subjected to diffusion processes but still conserve enough energy to escape from the surface of the sample will contribute to the background signal.

For all of these reasons, XPS spectroscopy is commonly used to investigate the chemical composition of a material surface, with a depth of about 10 Å. Moreover, this technique enables a rapid analysis of the sample, with a minor damage of the sample. In addition, every material that can be placed in an ultra-high vacuum ambient can be analysed with this technique. The technique is based on the photoelectric effect: a photon of well-defined energy, $h\nu$, strikes on a solid material, penetrating its surface and being absorbed by an electron of the material. If the photon energy is sufficiently high, the electron will emerge from the surface with a kinetic energy of:

$$E_k = h\nu - E_b$$

where E_b represents the binding energy of the electron in the solid.

X-ray source

In the XPS instruments the X-ray source are the emission lines of a metallic target (anode) subjected to electron bombardment with electron energy in the order of tens of KeV. Sources can be equipped with one or two anodes. In both source types, a filament able to carry a current is placed near the anode and emits electrons via thermoionic effect. The anode is usually settled with a positive potential respect to the filament, and attires the electrons emitted from the filament which will strike on the metallic target (anode) and will determine the X-ray emission with characteristic energy from the

anode. During the bombardment process only 1 % of incident electrons' kinetic energy is converted in X-rays while the remaining energy is converted in heat. For this reason, it is necessary to constantly cool down the target with deionized water.

To eliminate the background, the source is separated from the rest of the system by an aluminium window.

The anodes equipped on the source used in these experiments are aluminium ($K_\alpha = 1486.6$ eV) [58] and magnesium ($K_\alpha = 1253$ eV) [58] because these two materials guarantee characteristic peaks with energy able to excite the deep core level of all elements of periodic table. For both the anodes, the emission spectrum is composed of one or more characteristic lines that results from the electronic transitions toward the internal holes created by the incident electrons, superimposed to a continuum background due to Bremsstrahlung radiation. These components contribute to the overall dose of radiation that invest the sample, determining an increase of background signal, peaks enlargement and a certain grade of damage of the surface. In order to overcome this problem, it is possible to use monochromatic sources constituted of only one line of the pair $K_\alpha 1/2$. The principle used is the dispersion of X-rays via diffraction on a crystal: radiations with different wavelength are diffracted at different angles, in accord with Bragg law:

$$n\lambda = 2dsin\Theta$$

where n is the diffraction order, λ is the wavelength of X radiation, d is the distance between two crystal planes and Θ is the Bragg angle. Commonly used materials in these system ($2d = 8.5$ Å) are quartzs, the Al- K_α line is at $\lambda = 8.3$ Å, and the first diffraction order is at $\Theta = 78.5°$. The angle between incident and diffracted rays must be 23° [59]. To focus the monochromatic beam on the sample, all the components (source, crystals and sample) must be placed on three points on a Rowland circumference. The linewidth can be then reduced to values smaller than $\Delta = 0.3$ eV [59]. In fig. 2.4 are listed some important parameters (excitation energy, relative intensities and linewidth) of some materials commonly used as anodes. In fig. 2.5 are listed the energy shifts and the relative intensities of satellite peaks for the primary excitation.

    The low-energy X-ray excitation lines (Y M_ζ, Zr M_ζ) are attractive for both the energies, respectively at 132 eV and 151 eV, and their natural linewidth are, respectively, 470 meV and 770 meV. The radiation energies have values comprised between Al/Mg K_α and the almost monochromatic UV excitation. The minimum distance between the anode centre and the sample is around 14 mm, moreover the anode and its internal water tube are interchangeable [60].

Element and Line	Excitation Energy (in eV)	linewidth (in meV)
Mg $K_{\alpha 1/2}$	1253.64	680
Al $K_{\alpha 1/2}$	1486.65	850
Zr M_ζ	151.4	770
Y M_ζ	132.3	470
Si K_α	1739.5	1000
Cu L_α	929.7	3800
Zr L_α	2042.4	1700
Ag L_α	2984.4	2600

Figure 2.4: Excitation energies and lines of the main X-ray anode materials
[60]

Line	Energy shift (in eV) Mg	relative Intensity (in %) Mg	Energy shift (in eV) Al	relative Intensity (in %) Al
$K_{\alpha 3}$	8.4	8.0	9.8	6.4
$K_{\alpha 4}$	10.1	4.1	11.8	3.2
$K_{\alpha 5}$	17.6	0.6	20.1	0.4
$K_{\alpha 6}$	20.6	0.5	23.4	0.3
K_β	48.7	0.5	69.7	0.6

Figure 2.5: Mg/Al K_α satellites
[60]

Vacuum conditions necessary for the operation of X-ray source

Even though the X-ray source can work for pressure values around $7.5 * 10^{-6} Torr$, higher vacuum conditions (10^{-9} Torr or lower) are strongly recommended in order to prevent the contamination of the X-Ray window and the space surrounding the anode.

Moreover, good vacuum conditions prevent the oxidation of the filament during the use, thus leading to a long-life duration of both the anode and the window. This will also reduce the risk of having sparks between the anode and the parts connected to the ground, and enable the operation of the X-ray source for longer times at its maximum intensity.

Separate pumping

The X-ray source used in this Ph.D. project (Specs GmbH, X-ray source XR-50) is equipped with a differentiate pumping realized with a ionic pump, which allows to have better vacuum condition in the space surrounding the anode, especially during the degassing process of the system.

Moreover, it helps reducing the ageing of both the anode and the aluminium window.

Description of X-ray source

The mechanical parts of the X-ray source used in this Ph.D. project are depicted in figure 2.6 and are briefly described in the followings [60]:
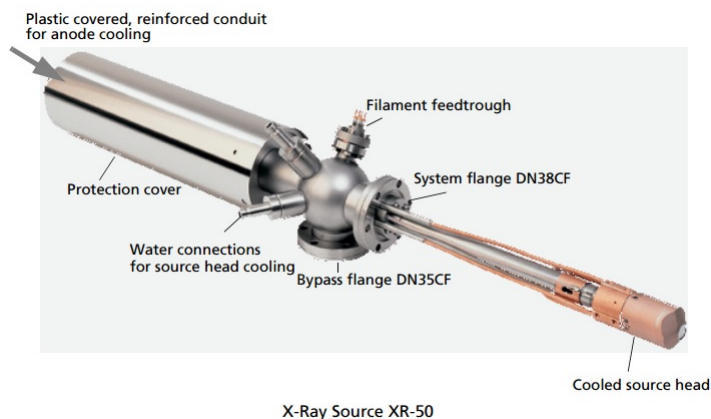
Figure 2.6: X-Ray source XR-50 [60]

- Principal compartment of the source with overture for differentiate pumping, a 4 pin bypass to connect the cathode to the high voltage source, and connecting flanges to cool down the cathode and the external cover of water chiller.

- principal frame of x-ray source with source head, cage anode and fixed support for the refrigerated copper tank.

- Two opposite refrigerant tanks.

- Assembling of the cathode with the filament (see fig. 2.7).

- Double anode covered with aluminium and magnesium.

- Internal water pipe in the anode with quick fit connection flanges for the water refrigeration of the anode.

- Anterior copper cone with window of the X-ray source made of a alumina foil.

- Ceramic flange to insulate the anode of the source and the water pipe.

29
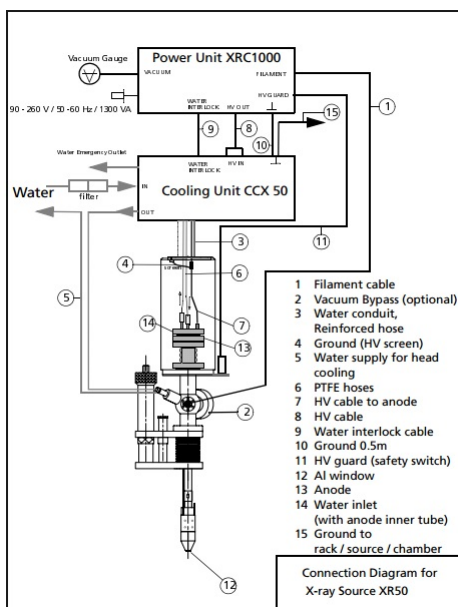
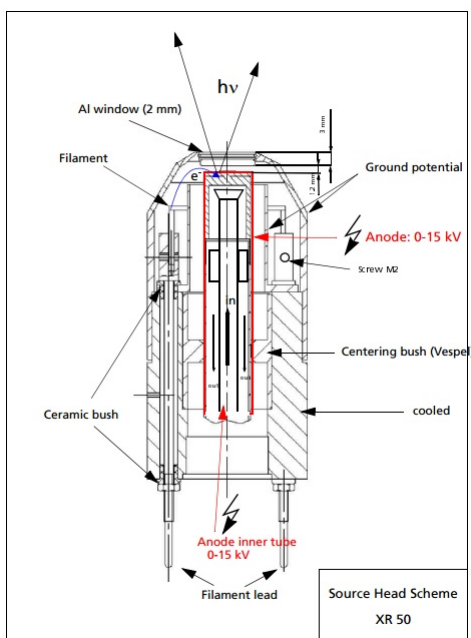Figure 2.7: Connection diagram for X-Ray source XR-50 [60]

Figure 2.8: Source head scheme XR-50 [60]

2.5 Optical Characterization

Optical absorption is the capacity of a material to absorb the energy associated to the electromagnetic radiation propagating inside the material itself [61].

The absorption takes place by means of energy transfer from the incident radiation to electrons, atoms or molecules of the material. The absorption depends from the material and the frequency of the incident radiation. By studying the absorption spectrum, therefore, it is possible to identify the atoms and molecules that compose the studied material.

In particular, the UV-VIS optical absorption involves the absorption of light radiation in the visible region (350-700 nm) and the near UV region (200-350 nm). The absorption of this radiation by molecules of the material causes some energetic transition of valence electrons, regardless of whether they are free or bonded to atoms. The spectra collected in the visible region are also called "band spectra" because they also show rotational and vibrational transitions lines so close to each other that they appear as continuous (a band exactly) and are generally due to more or less largely delocalized π-bonds electrons.

In this thesis work a Horiba Jobin Yvon Olympus microscope was used with 10x, 50x, and 100x lenses. The microscope was equipped with a UV-VIS source and a Triax 320 (Horiba Jobyn Yvon) spectrometer working in the 200 -1500 nm range for optical signal processing (fig. 2.9).
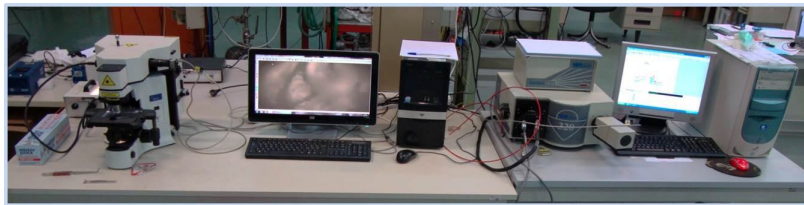

Figure 2.9: Optical characterization apparatus

The optical detection system consists of a monochromator connected in series to a CCD. The monochromator is a tool with two slits, placed at the input and the output, respectively. The input slit collects the light signal coming from the sample. The output slit transfers the signal to the CCD. The sample was placed on the specific holder of the microscope and focused by the 100X lens via a camera connected to a computer. Once the sample was focused, a UV beam was sent normally to the sample surface. The signal was then collected by the 100x lens and sent to the optical system connected to the spectrometer input slit via optical fiber. The monochromator consists of toroidal mirrors that focus the input signal on a grating tower where 3 different diffraction patterns are housed (each analysing wavelengths ranging from UV to IR spectrum). These mirrors decompose the signal in

31

its components at various wavelengths. The tower is remotely controlled via software, allowing the choice of the most suitable diffraction pattern for the incoming spectra analysis. Once the signal comes out the grating tower, it is picked up by another toroidal mirror and sent to the CCD.

The CCD detector is a SI wafer with a resolution of 1024 x 128 pixels that transforms the incoming optical signal into an electrical signal due to the photoelectric effect. For each sample, a deposit on a glass substrate has been made by using a simple evaporation and drying process The samples placed on the holder were illuminated using a white led, to permits the acquisition of both the transmitted spectra $I_t(\lambda)$ and reflected spectra $I_r(\lambda)$. The extinction cross section $\varepsilon(\lambda)$, the transmittance t(λ) and the reflectance r(λ) were calculated as function of length d then using the relationships:

$$\varepsilon(\lambda) = -Log\frac{I_t(\lambda)}{I_\epsilon(\lambda)}$$

$$t(\lambda) = \frac{I_t(\lambda)}{I_\epsilon(\lambda)}$$

$$r(\lambda) = \frac{I_r(\lambda)}{I_\epsilon(\lambda)}$$

where $I_\epsilon(\lambda)$ represents the source spectrum. The total transmittance (t) and reflectance (r) were obtained by numerical integration of the transmission and reflection spectra, while the total absorbance (a) was calculated using the equation:

$$a + t + r = 1$$

The particle concentration inside a colloidal solution was evaluated following the Lambert and Beer's Law:

$$a = c\alpha l$$

where c is the particle concentration, α is the molar extinction cross section and l is the optical path length of the experimental setup.

Chapter 3

Counter Electrodes in DSSCs

The use of MWCNT to replace the platinum as counter electrode was already discussed in the State of art section. However, it is still possible to further boost the performance of these materials by decorating them with metal nanoparticles. The choice of the transition metal to be used for this decoration is crucial.It must have a good resistance to the corrosive action of the electrolyte solution still maintaining high catalytic properties. Among all the possible transition metals, we focused our attention on Nickel and the Cobalt-Nickel alloy. These two particular materials, in fact, posses a good resistance to the corrosive action of the electrolyte solution, as reported by [62, 63, 29].

The decoration of MWCNT by using metal nanoparticles is usually a long and quite complicate process which involves the synthesis of such nanoparticles through chemical processes [23, 25, 26] and their consequent deposition on the MWCNT surfaces, or their synthesis directly *in-situ* on the MWCNT [29].

Our approach follows a completely different methodology, focusing on the in-situ decoration of MWCNT by means of a laser technique. Compared with the traditional chemical techniques, this approach permits to obtain a uniform decoration of the MWCNT strongly reducing the time necessary for the deposition and avoiding the use of polluting chemical reagents.

3.1 Decoration of MWCNT with Ni or Co-Ni nanoparticles via PLD

The method we use to prepare the counter electrodes is quite simple when compared with the traditional chemical techniques, as stated before. The MWCNT used in this work are a commercial powder of carbon nanotubes purchased from Raymor-Nanointegris, with a nominal purity $> 99\%$, an average inner diameter of 4 nm, an average outer diameter < 20 nm, and a length of 1-12 micrometers. A 0.3 mg/mL suspension of MWCNT in

dimethylformamide (DMF) was obtained by sonicating them for 2 hours, and the obtained suspension was finally deposited via spray-coating on FTO glass. During the spray-coating process, the substrate was maintained at a constant temperature of 200 °C to facilitate the solvent evaporation.

To decorate the MWCNT with the Ni or the CoNi nanoparticles via PLD, the samples were mounted inside a vacuum chamber on a sample holder placed at 5.5 cm of distance from the Ni or CoNi target. Both holders were kept rotating (5rpm) to ensure a uniform coverage of the substrate. The KrF excimer laser parameters used during the deposition are the following: wavelenht of 248 nm, pulse duration of 14 ns, repetition rate of 20 Hz and laser energy of 140 mJ/pulse. The angle between the laser beam and the Ni or Co-Ni target was 45°, the deposition was performed in inert atmosphere using a 300 mTorr pressure of Helium (He). The number of laser pulses used for the PLD deposition was varied from 5000 to 60000 for the Nickel, and from 10000 to 60000 for the CoNi in order to obtain different coverage rates of the MWCNT surface and to study the effect of the decoration on the photovoltaic performances of the counter electrode.

The obtained counter electrodes were assembled together with commercial TiO$_2$ photoanodes (Dyesol) previously sensitized with N719 dye and the space between the two electrodes was filled using a I$^-$/I$_3$ $^-$ electrolyte solution (EL-HPE, Dyesol)

3.2 Morphological characterization

The morphological characterization of the Ni/MWCNT and CoNi/MWCNT counter electrodes was performed by using a STEREOSCAN scanning electron microscope (SEM) working at 20 KeV in both Back Scattering Emission (BSE) and Secondary Electron Emission (SE). The bulk composition was investigated by using an EDX spectrometer after the image acquisition.

The root-mean-square (RMS) roughness of the surface, which is another critical parameter that influences the catalytic performances of the material, was evaluated by using Nanoscope software after taking the AFM images via an ICON Atomic Force Microscope (Bruker) in tapping mode.

3.2.1 SEM characterization

The morphology comparison between the pristine MWCNT CE and the PLD-decorated ones is shown in fig. 3.1.

The first noticeable difference is that the pristine MWCNT appears as a disordered pattern of MWCNT, while in both CoNi/MWCNT and Ni/MWCNT the carbon nanotubes are completely wrapped by the metal nanoparticles, creating a highly porous structure. Moreover, by increasing the number of laser pulses (NLP) used during the PLD deposition, it is possible to observe an increase of the surface coverage: for low NLP the
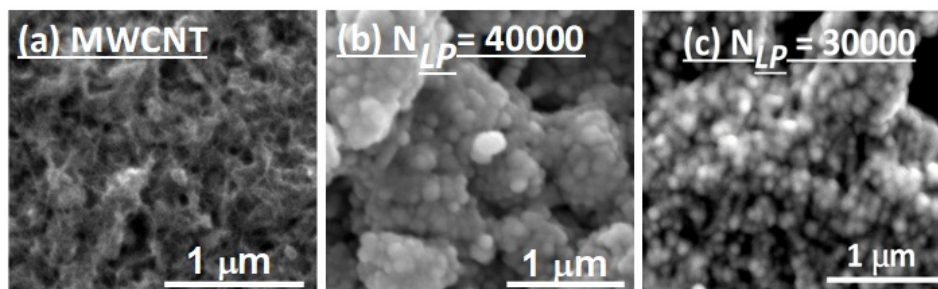
Figure 3.1: top-view SEM image of the (a) pristine MWCNTs, (b) Co-Ni/MWCNTs ($N_{LP} = 40000$), (c) Ni/MWCNTs ($N_{LP} = 30000$).

MWCNT are not completely covered by Ni or CoNi nanoparticles (fig. 3.2, panels a and c) whereas at high number of laser pulses the MWCNT are uniformly covered by the Ni or CoNi nanoparticles and it is no longer possible to distinguish the nanotubes' shape (fig. 3.2, panels b and d).

Another noticeable difference is the increase of the nanoparticles' size as a function of the number of laser pulses. In fig. 3.3 it is shown the variation of the CoNi nanoparticles' size as a function of the number of pulses. It is evident how, by varying the N_{LP} from 500 to 10000, the average particles size increases from 28 to 120 nm; for $N_{LP} \geq 10000$, the average diameter of the nanoparticles remains almost constant and saturates around this value of about 120 nm.

The progressive accumulation of nanoparticles on the MWCNT due to the increase of the number of laser pulses used, causes the formation of cauliflower-like aggregates with a consequent increase of the material porosity. However, on the other hand, the presence of big aggregates on the surface may increase the contact resistance between the counter electrode and the electrolyte solution, influencing negatively the electron transfer. For both Ni and CoNi, we found two optimized values of N_{LP} that ensure a uniform coverage of the MWCNT and the formation of cauliflower-like aggregates of small or medium dimensions. The presence of these aggregates on the surface is important to increase the specific surface area of the CE without excessive contact resistances. Since both Co and Ni are well known catalyst [64, 65], it is important to have a porous structure covered with these metals nanoparticles because it can enhance the electron transfer to the electrolyte solution.

3.2.2 AFM characterization

The surface topography and the local surface roughness of both Ni/MWCNT and CoNi/MWCNT counter electrodes was evaluated by AFM analysis.

The variation of N_{LP}, as introduced before, causes a variation of morphology of the counter electrodes, with a progressive accumulation of material
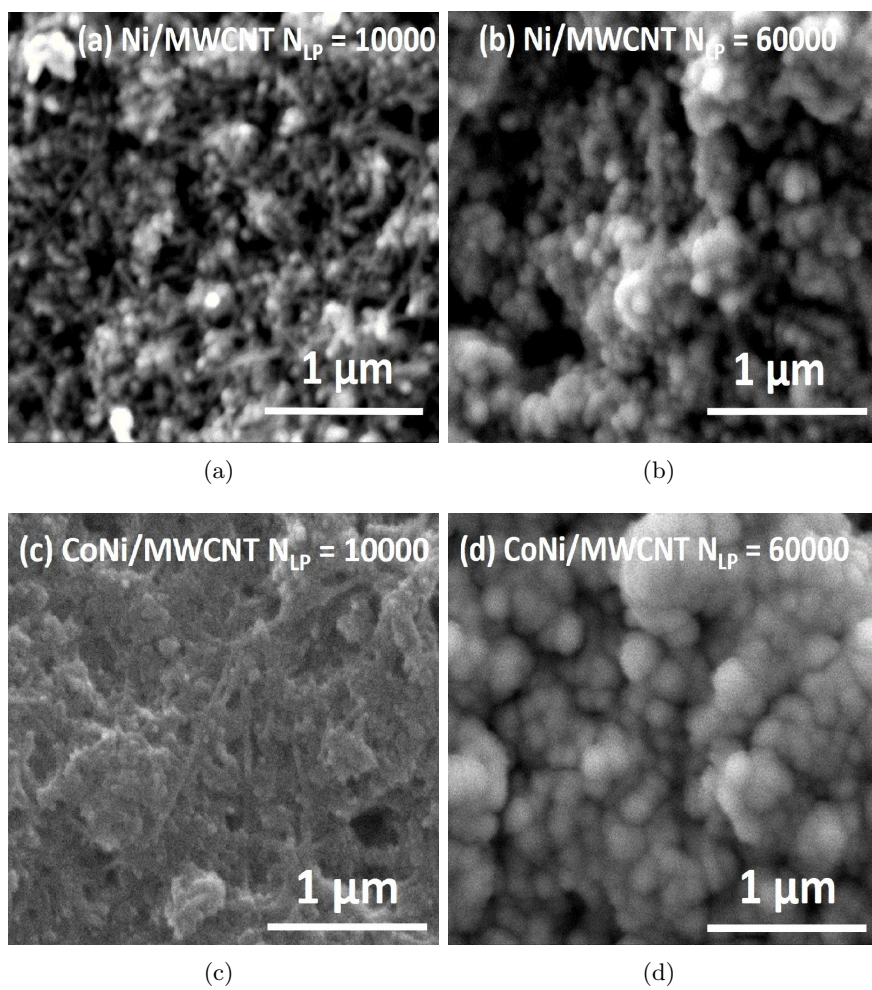
Figure 3.2: SEM image of the (a) Ni/MWCNT (N_{LP} =10000), (b) Ni/MWCNTs (N_{LP} = 60000), (c) CoNi/MWCNTs (N_{LP} = 10000), (d) CoNi/MWCNTs (N_{LP} = 10000).
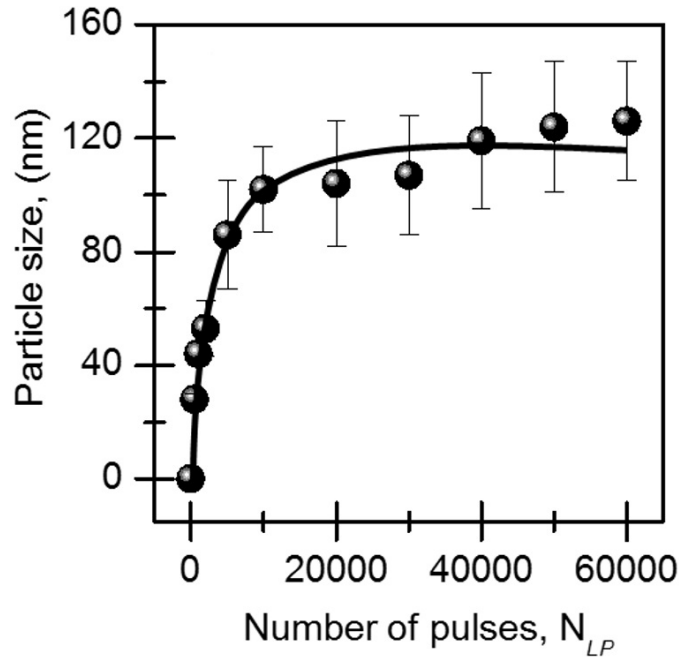
Figure 3.3: Variation of average particle size of the Co-Ni nanoparticle layer after their decoration on to the MWCNTs as a function of N_{LP}.

and the consequent formation of bigger aggregates of nanoparticles. The AFM images (2D and 3D) obtained for both the CoNi/MWCNT (fig. 3.4) and the Ni/MWCNT (fig. 3.5) at different N_{LP} are shown below.

First of all, by comparing the 2D and the 3D images taken at low number of laser pulses with the images obtained from the samples PLD-decorated at high number of laser pulses it is possible to observe the evolution of the coverage of MWCNT (figures 3.4 and 3.5). For both Ni and CoNi, in fact, at low N_{LP} the surface appears to be mainly constituted of small nanoparticles which completely wrap the carbon nanotubes (fig. 3.4 c,d and fig. 3.5 a,b). In some cases, the shape of the carbon nanotubes is still clear under the nanoparticles and, in some zones, the MWCNTs are not perfectly covered. By increasing the N_{LP}, it is possible to see the progressive accumulation of these nanoparticles, and the formation of the cauliflower-like aggregates already discussed in the SEM section. From the 3D images (3.4 d,f,h and 3.5 b,d,f,h, in particular, it is possible to appreciate the progressive loss of the fine structures of these aggregates, due to the gradual increase of the nanoparticle size. While at N_{LP}=40000 both Ni/MWCNT and CoNi/MWCNT appear as aggregates made of small nanoparticles, at N_{LP}=60000 the surface is fully covered with big aggregates. The whole surface is less porous, if compared with the previous images.

The formation of these aggregates on the samples' surface can be explained
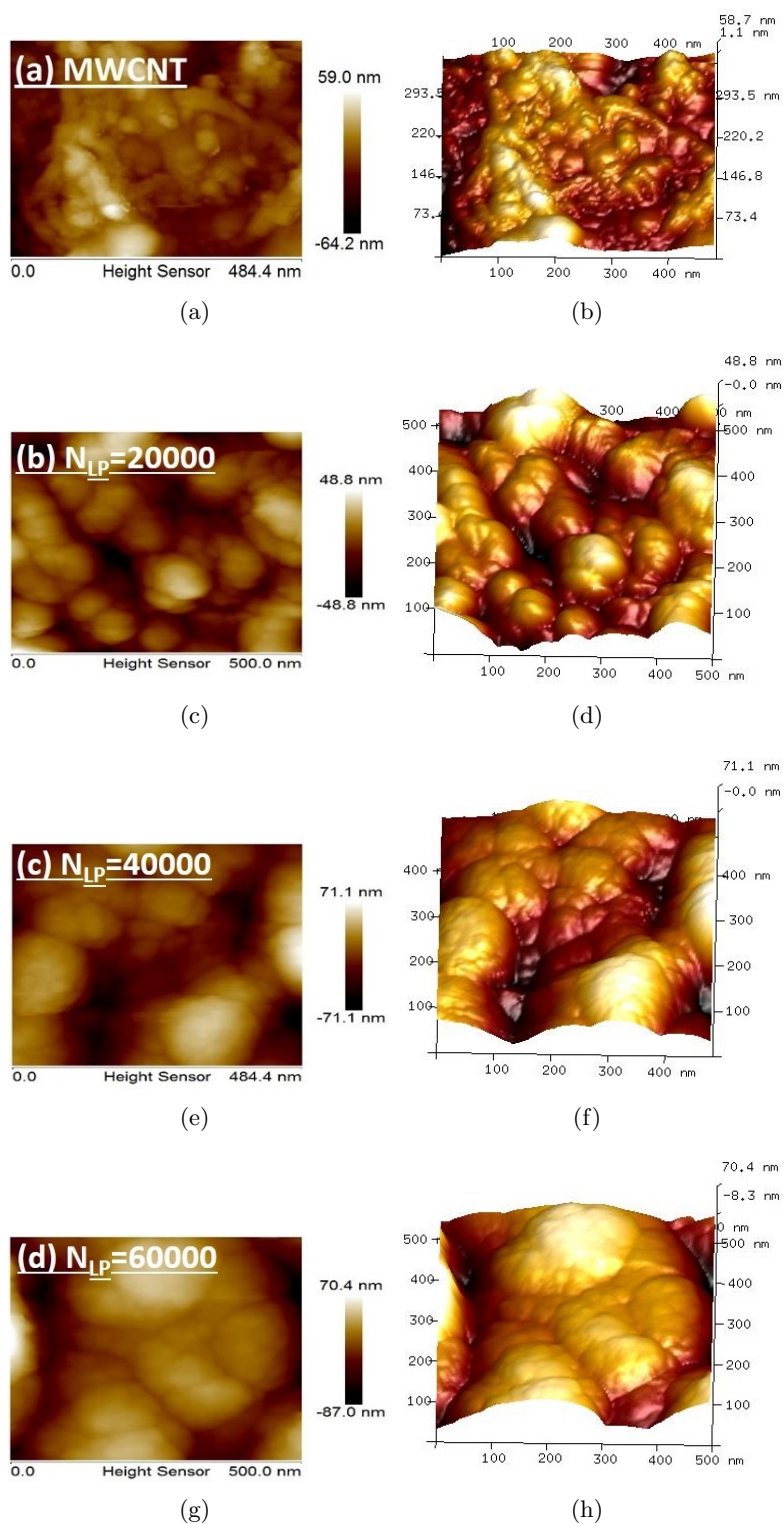
(a)

(b)

(c)

(d)

(e)

(f)

(g)

(h)

Figure 3.4: 2D (a,c,e,g) and 3D (b,d,f,h) images of CoNi/MWCNT at different N_{LP}.

5000 NLP

(a)

(b)

20000 NLP

(c)

(d)

40000 NLP

(e)

(f)

60000 NLP

(g)

(h)
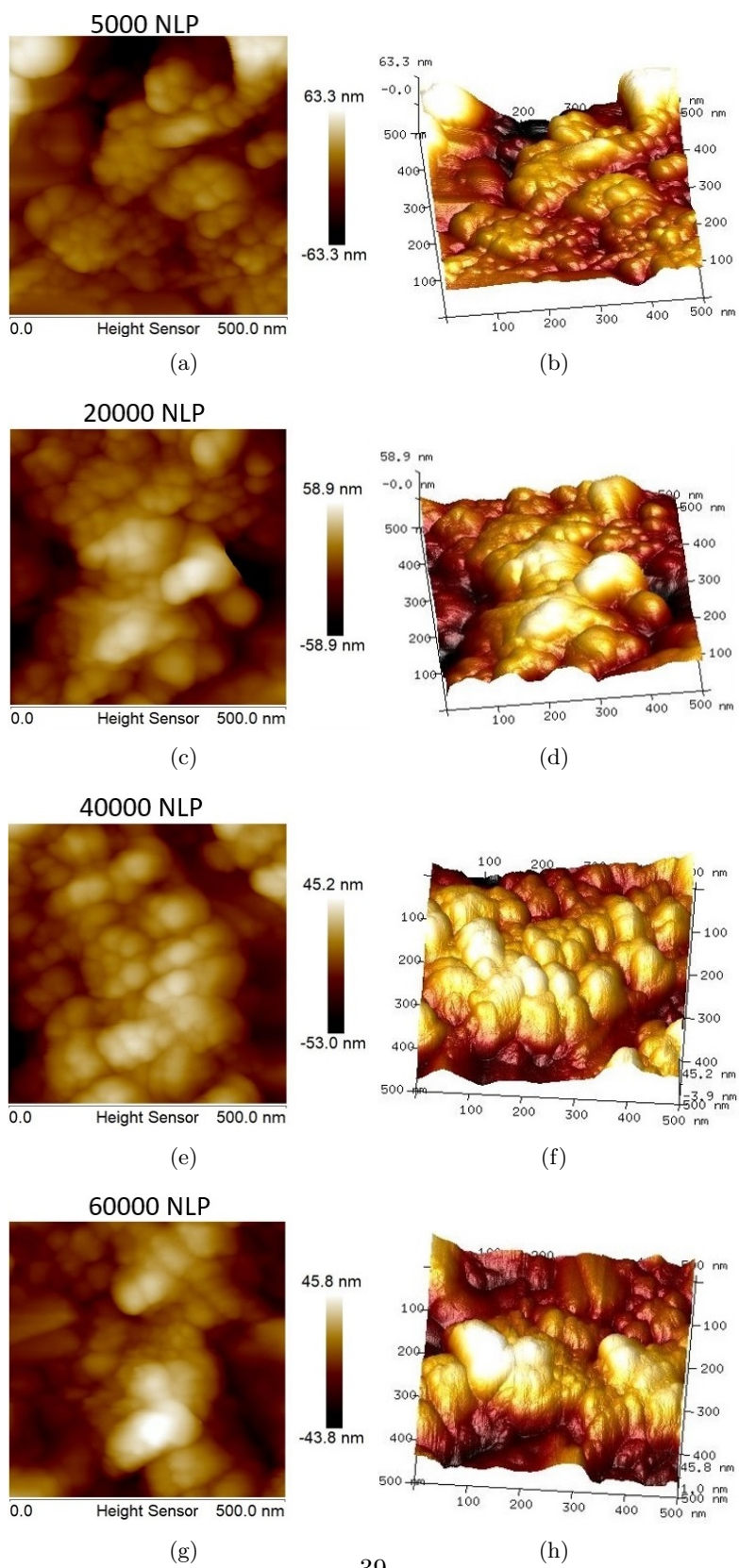
Figure 3.5: 2D (a,c,e,g) and 3D (b,d,f,h) images of Ni/MWCNT at different N_{LP}.

N_{LP}	roughness (nm)	St. Dev
0	25	4
500	28	6
10000	30	6
20000	37	8
30000	40	9
40000	42	12
50000	37	10
60000	31	5

Table 3.1: local surface roughness of CoNi/MWCNT decorated with different N_{LP}

N_{LP}	Roughness (nm)	St. Deviation (nm)
5000	15.8	0.2
20000	8.8	0.6
40000	15.5	0.7
60000	13.2	0.1

Table 3.2: local surface roughness of Ni/MWCNT decorated with different N_{LP}

with the Young's theory [66] taking in to account both the nucleation that takes place during the PLD decoration and the wetting properties of materials involved in the process. According to this theory the nucleation rate depends on the metal cohesion energy, on the metal-substrate interface energy, and on the diffusion barrier value. The wetting phenomenon depends, instead, on the interplay between the metal-substrate interface energy and the metal surface energy. It is known that the aggregation phenomenon takes place when the metal surface energy (E_s) is greater than the metal-substrate interface energy (E_f), and the diffusion barrier (E_{diff}) has a lower value [67]. Moreover, both Co and Ni nanoparticles synthesized via laser ablation technique in solution, tend to cover uniformly the CNTs with local layer-like growth, as reported in [68], and thus the contemporary presence of nanoparticles uniformly distributed and a local formation of aggregates is due to the close value of E_s and E_f and to the relatively high E_{diff} of both Co and Ni. The progressive loss of the aggregate fine structures was confirmed by the local surface roughness measurements shown in fig. 3.6 and tables 3.1 and 3.2.

As evidenced in fig. 3.6, for both CoNi (panel (a)) and Ni (panel (b)), the variation of the local surface roughness strongly depends on the N_{LP} used during the PLD deposition process. The roughness, in fact, increases for the CoNi/MWCNT from 25 nm at $N_{LP} = 0$ (pristine MWCNTs), to its maximum value of 42 nm for the film decorated with $N_{LP} = 40000$ and then
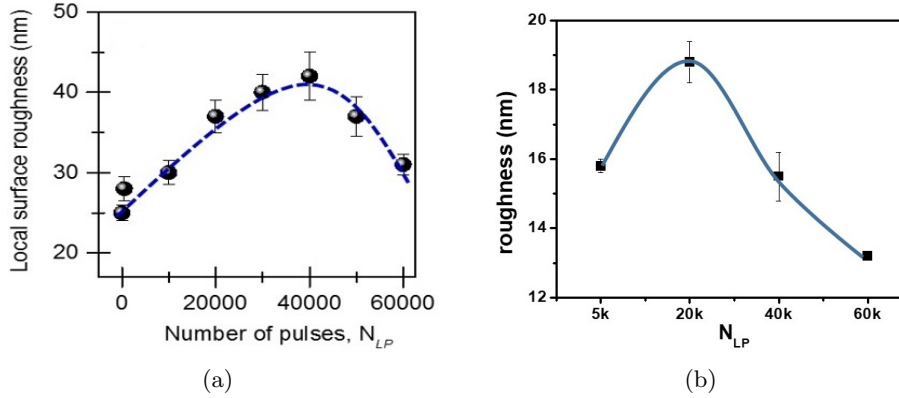
Figure 3.6: Variation of local surface roughness of the PLD-decorated CoNi/MWCNTs (a) and Ni/MWCNT (b) as a function of N_{LP}.

decreases to 31 nm at $N_{LP} = 60000$. A similar behaviour is found for the Ni/MWCNT for which the roughness increases from 15.8 nm at $N_{LP} = 5000$ to its maximum of 18.8 nm at $N_{LP} = 30000$, and then decreasing to 13.2 nm at $N_{LP} = 60000$. This increase of local surface roughness at low number of laser pulses is particularly important to enhance the catalysis process that takes place at the interface between the CE and the electrolyte solution. In the J-V characterization section will be shown the impact of this parameter on the photovoltaic performances of these DSSC devices.

3.3 Chemical Characterization

The chemical characterization of the Ni/MWCNT and CoNi/MWCNT counter electrodes was performed by using an ex-situ X-ray Photoelectron spectrometer (XPS - Spectra Instruments) working in ultra high vacuum (UHV) condition at a pressure of 10^{-9} Torr; the excitation source used was a monochromatic Mg-Kα X-ray source ($h\nu = 1253.64$ eV), and the spectra were calibrated by using the C 1s peak of a pure carbon sample (binding energy position of 284.6 eV) as reference. All the spectra were fitted by using CasaXPS software by adopting a Gaussian-Lorentzian peak shapes, after applying a Shirley background subtraction. The ultraviolet photoelectron spectroscopy (UPS) was performed with an ESCALAB 220iXL spectrophotometer. The excitation source used was a He discharge lamp (He I line, $h\nu = 21.2$ eV) working in normal emission with a resolution of 0.06 eV. The Fermi level of the materials was evaluated by using the gold one ($\phi = 5.0$ eV) as a reference value, and applying a -3 eV bias to eliminate the intrinsic detector work function barrier.

3.3.1 XPS measurements

The XPS technique was used to investigate the chemical composition and bonds of both Ni/MWCNT and CoNi/MWCNT surface. Fig. 3.7 shows the high resolution core level XPS spectral regions of Ni 2p (panel a) and Co 2p (panel b) of the CoNi/MWCNT decorated at $N_{LP} = 40000$ and of the Ni/MWCNT decorated at $N_{LP} = 20000$ (panel c).

All the spectra aquired show a complex structure with intense shake-up satellite signals located at higher Binding Energy (BE) with respect to the main peak. These satellites are due to the multi-electron excitation processes, as reported in [69]. The Ni 2p and Co 2p core level spectra for both CoNi/MWCNT and Ni/MWCNT (fig. 3.7) were deconvoluted in different peaks. For the nickel in CoNi/MWCNT (fig. 3.7 panel a), the Ni $2p_{3/2}$ was deconvoluted in 5 peaks with BE of 853.7 eV for the main peak, and 855.4 eV, 860.9 eV for the satellites; these value are typical of the NiO, as reported in [70]. The two small peaks at 864.4 eV and 866.3 eV respectively are negligible and not identifiable.

Similarly, for the nickel in Ni/MWCNT (fig. 3.7 panel c) the Ni $2p_{3/2}$ spectrum can be deconvoluted in three peaks at BE of 853.2 eV for the main peak, 855.9 eV and 859.7 eV for the satellites. The Ni $2p_{1/2}$ was deconvoluted into three peaks too, with the main one centred at 870.5 eV of BE, and the satellites located at 872.2 eV and 877.4 eV .

The Co $2p_{3/2}$ spectrum for the CoNi/MWCNT counter electrode was deconvoluted in five peaks, with the main one centred at 779.6 eV and the satellites located at 781.7 eV, 785.1 eV and 786.1 eV. For Co $2p_{3/2}$ these peaks position are typical of CoO, as reported in [70] . Finally, the O 1s spectrum was acquired for both the CoNi/MWCNT (fig. 3.8 (a)) and the Ni/MWCNT (fig. 3.8 (b)).

The O 1s of CoNi/MWCNT (fig. 3.8 (a)) was deconvoluted in two peaks located at about 529.8 eV and 531.9 eV. The first peak is typical of the metal oxygen bond and can be addressed to both Ni-O [69] and Co-O [70], whereas the second peak is due to O-H bonds and can be addressed to the surface hydroxyl groups [71].

The O 1s of Ni/MWCNT (fig. 3.8 (b)) was deconvoluted in three peaks, located at about 529.3 eV, 531.2 eV and 534.6 eV. Even in this case, the peak positions are typical of Ni-O bond, as reported by [70]. The presence of Co-O and Ni-O on the surface of both the two different kind of counter electrodes can be explained by means of the interaction of Ni and Co with the atmospheric oxygen in proximity of the MWCNTs surface. The presence of these transition metals oxides on the surface of the nanoparticles is very important to enhance the catalysis of iodine-based electrolytes. In fact NiO easily interacts with the ions of the electrolyte solution due to its ionic feature [72]. The CoO reduces the resistances at the interface between the CE and the electrolyte solution, improving the electron transport and enhancing the
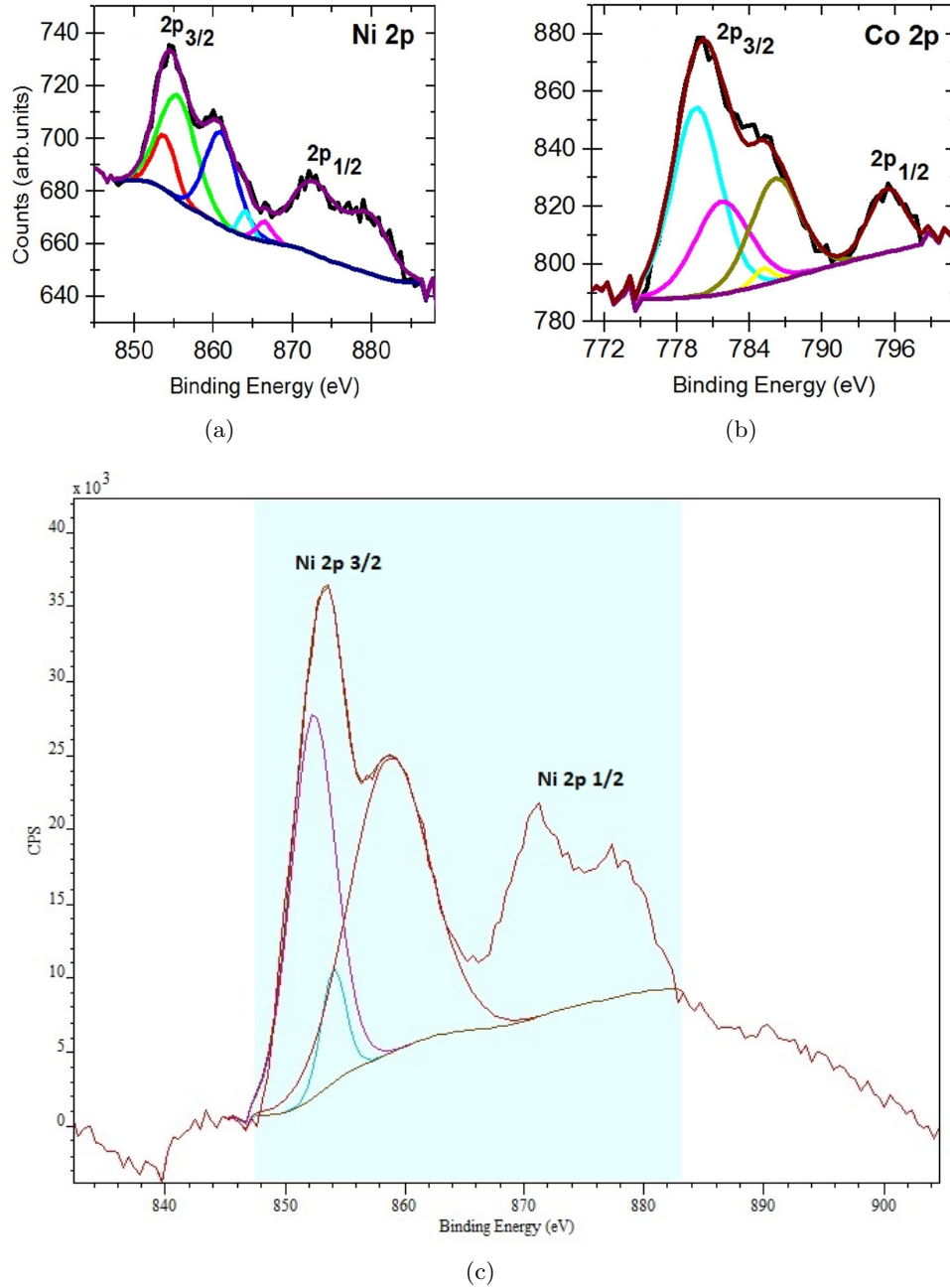
(a)

(b)

(c)

Figure 3.7: XPS spectra of Ni 2p (a) and Co 2p (b)of CoNi/MWCNT counter electrode decorated at N_{LP}= 40000, and Ni 2p of Ni/MWCNT counter electrode decorated at N_{LP}= 20000 (c).
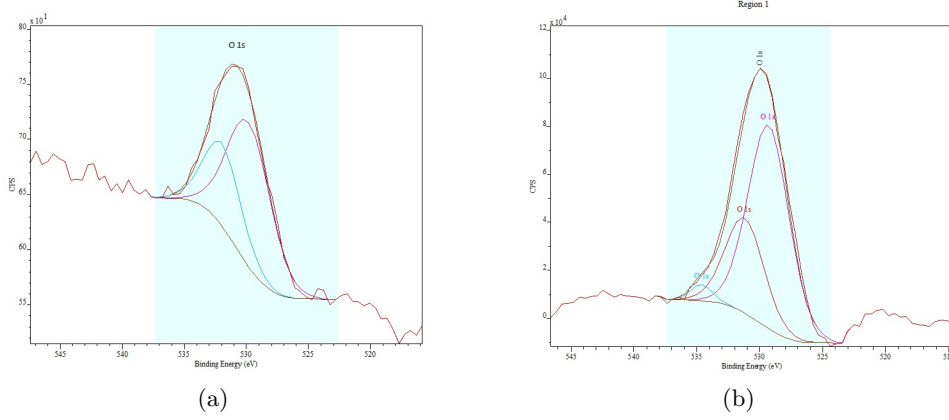
(a)   (b)

Figure 3.8: XPS spectra of O 1s of CoNi/MWCNT CE decorated at $N_{LP}=$ 40000 (a) and of Ni/MWCNT CE decorated at $N_{LP}=$ 20000 (b)

Element	Wt %	At %	K-Ratio	Z	A	F
C	2.29	9.48	0.0076	1.2295	0.2684	1.0003
O	3.51	10.92	0.0262	1.2000	0.6191	1.0023
Co	47.51	40.08	0.459	0.9659	1.0000	1.0000
Ni	46.68	39.52	0.4661	0.9982	1.0003	1.0000

Table 3.3: EDX element percentage analysis on CoNi/MWCNT counter electrodes.

photovoltaic performances of these DSSC devices [63]. An EDX analysis was also performed for the CoNi/MWCNT counter electrode in order to determine the bulk composition of the nanoparticle layer. The EDX spectrum showed in fig. 3.9 evidences the predominant presence of both Co and Ni at average weight percentages of 47.5% and 46.7% respectively, with also minor contributions of C (2.3%) and O(3.5%). The elements quantitative analysis is reported in tab. 3.3

3.3.2 UPS measurements

The UPS measurement was carried out in order to determine quantitatively the variation of the work function (Φ) of the CoNi nanoparticle film since it is an important information to investigate the enhancement of electron transfer from the counter electrode to the electrolyte solution.

The work function is defined as $\Phi(eV) = h\nu - (E_{cut-off} - E_{Fermi})$ [73] where E_{Fermi} is the Fermi edge and the half height of the secondary electron cut-off region, whereas the secondary electron cut-off region can be derived by linear extrapolation of the edge. The reference used for the calibration was a gold sample with work function $\Phi_{Au} = (5.0 \pm 0.1)$ eV.
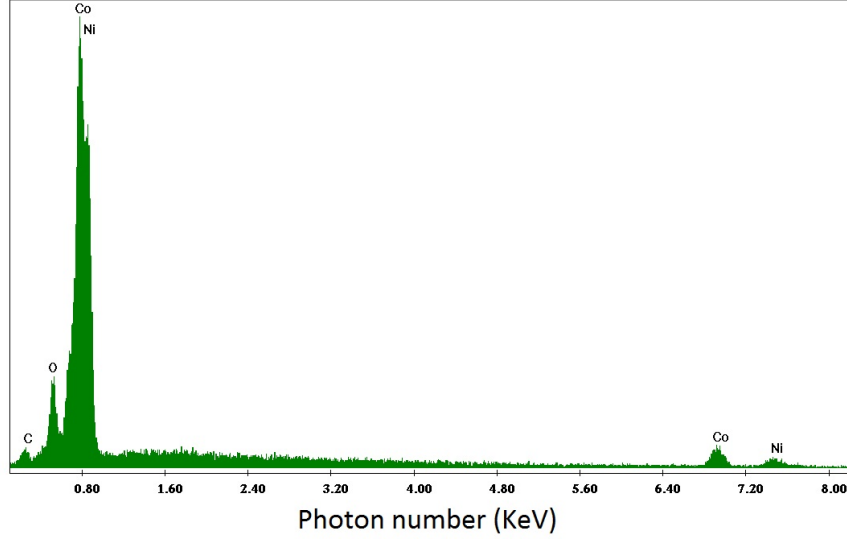
Figure 3.9: EDX measurements of element percentage on CoNi/MWCNT (N_{LP} = 40000) CE, as example for all CoNi-decorated samples
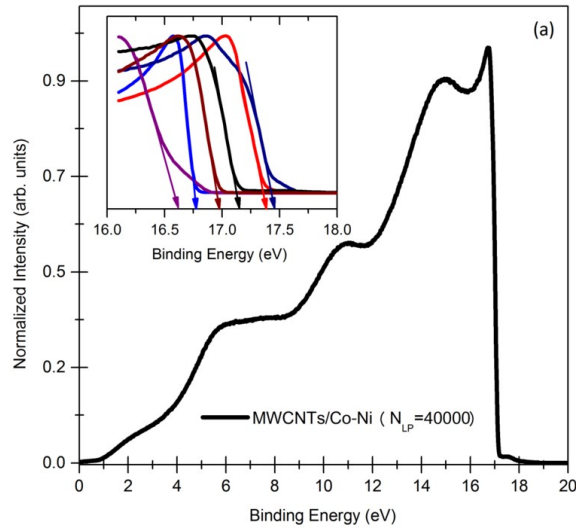

Figure 3.10: UPS spectrum of MWCNTs decorated Co-Ni nanoparticle layer deposited using $N_{LP} = 40000$ pulses. The inset shows the spectra of secondary electron cut-off region of different CEs: pristine MWCNTs (blue), Co-Ni/MWCNT $N_{LP} = 500$ (green), Co-Ni/MWCNT $N_{LP} = 40000$ (red), Co-Ni $N_{LP} = 40000$ (brown), platinum (black).
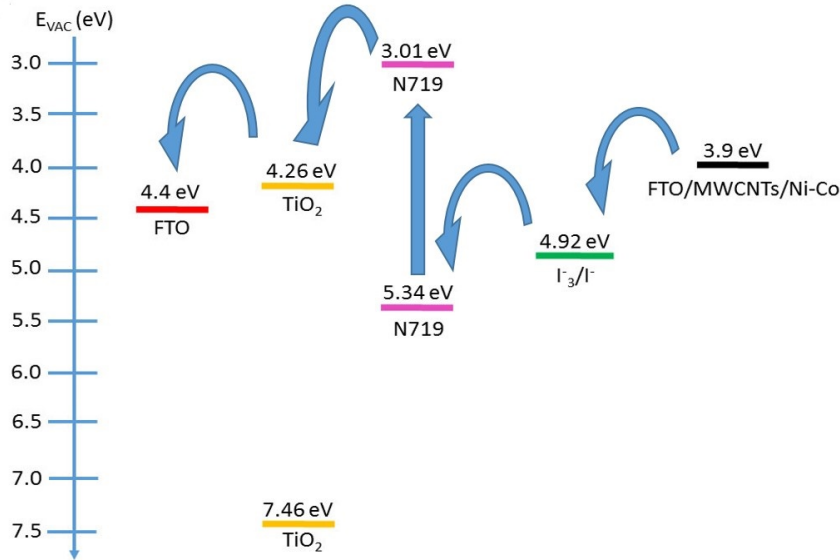
Figure 3.11: Schematic band alignment model for the entire system of the fabricated DSSC device.

In fig. 3.10 is shown the UPS spectrum acquired for the CoNi/MWCNT ($N_{LP} = 40000$). The secondary electron cut-off regions of different counter electrodes is showed in the inset.

It is particularly relevant how the variation of the N_{LP} used during the PLD-decoration causes a variation of the Φ of the material and hence a variation of the secondary electron cut off region of the UPS spectra. In fact, the work function value of the pristine MWCNTs is about 4.8 eV [74, 75], while the CoNi nanoparticles deposited via PLD with $N_{LP} = 40000$ have a work function of 4.0 eV. The FTO substrate, on the other hand, has a work function value of 4.4 eV, as reported in [76]. The work function of the Pt-sputtered/MWCNTs/FTO counter electrode (used as conventional counter electrode in DSSC) is 4.3 eV. The work function measured for the CoNi/MWCNTs/FTO decorated at $N_{LP} = 500$ has an higher value, it is 4.7 eV. However, a further increase in the number of CoNi nanoparticles wrapped on the MWCNT causes the work function to decrease. For the sample decorated at $N_{LP} = 40000$, in fact, the work function value is about 3.9 eV, which is closer to that obtained for pure Co-Ni than to the one of pristine MWCNTs. In literature in fact was reported that the electrons could transfer from the metal nanoparticles to the encapsulated carbon nanotubes surface, causing a decrease of the local Φ value [77]. The transfer of electrons inside a DSSC device assembled by using the PLD-decorated MWCNT counter electrode is shown in fig. 3.11.

The DSSC components energy levels proximity favours efficient charge carriers separation and their transfer throughout the entire device. The incident photons are absorbed by the dye molecules, causing the promotion of excited electron from the HOMO (5.34 eV) to the LUMO (3.01 eV) energy levels [78]. The redox potential of the I^-/I_3^- electrolyte solution, instead, is 4.92 eV according to [79]. The alignment of all the energy bands inside the working electrode forms a "cascade" structure in which the excited electron is injected from the LUMO band of the dye molecule to the conduction band of TiO_2, and it is then transferred to the FTO substrate. These electrons generated inside the photoanode are transferred to the counter electrode (cathode), flowing inside the CoNi/MWCNT/FTO electrode where the reduced local work function value enhances the catalytic activity of the MWCNT counter electrode [77]. From the counter electrode the electrons are readily transferred to the ions inside the electrolyte solution, catalysing the redox reaction that regenerates the dye molecules and thus enhancing the photovoltaic performance of the dye-sensitized solar cell.

The CoNi/MWCNT/FTO counter electrode decorated at $N_{LP} = 40000$ is the best candidate to replace the standard Pt-based counter electrodes inside the DSSC devices. This is thanks to the presence of two catalytic materials such as the MWCNT and the CoNi alloy nanoparticles, together with a high local surface roughness, due to the formation of the peculiar cauliflower-like topography of the counter electrode surface, and to the low work function value.

3.4   Photovoltaic characterization

The J-V curves of the DSSC assembled with different counter electrodes (CoNi/MWCNT decorated at different N_{LP}, MWCNT and standard Pt) were acquired by using a Keysight B2901A source-meter and all the DSSC devices were illuminated with an Oriel Sol3A solar simulator working in ambient atmosphere in both dark and standard illumination condition (AM 1.5) using an incident light power of 100 mW/cm^2. The Power Conversion Efficiency (PCE) and Fill Factor (FF) were calculated using the standard equations: $PCE = (V_{max} I_{max} FF)/P_l$ and $FF = (V_{max} J_{max})/(V_{oc} J_{sc})$

where P_l is the power of irradiating light, J_{max} and V_{max} are respectively the current density and the voltage at the maximum power, and J_{sc} and V_{oc} are respectively the short circuit current density and the open circuit voltage.

3.4.1   J-V curves measurement

The CoNi/MWCNT and the Ni/MWCNT counter electrodes PLD-decorated by varying the N_{LP} were assembled with commercial Dyesol TiO_2 working
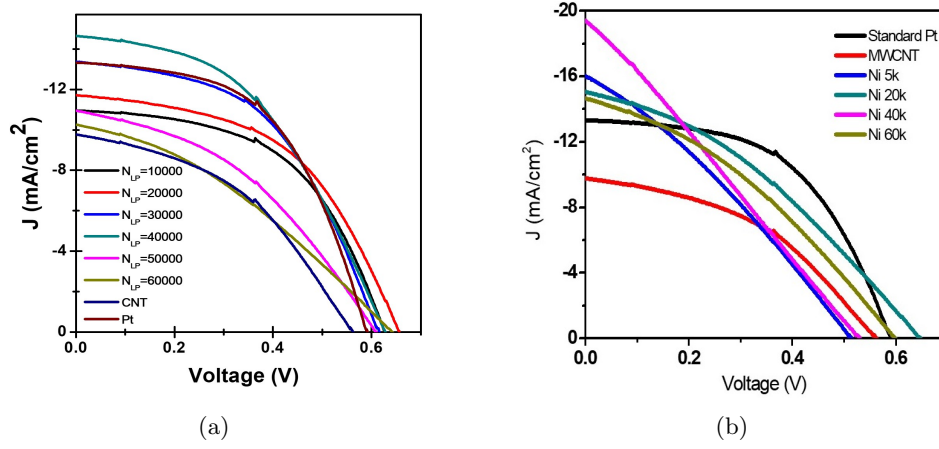
Figure 3.12: J-V characteristics of the DSSC devices made with pristine MWCNTs, standard reference Platinum (Pt) and (a) DSSC assembled by using Co-Ni/MWCNTs counter electrodes (N_{LP} ranging from 5000 to 60000), (b)DSSC assembled by using Ni/MWCNTs counter electrodes (N_{LP} ranging from 10000 to 60000)

electrodes (previously sensitized with N719 dye) in to DSSC devices. For each material, the J-V curves were systematically acquired and compared.

In figure 3.12 are reported the J-V characteristics of the CoNi/MWCNT (panel a) and Ni/MWCNT (panel b) counter electrodes made by varying the N_{LP} from 10000 (5000 for the Ni/MWCNT) to 60000. These novel counter electrodes are then compared with the pristine MWCNT counter electrode and with the standard Pt counter electrode. All the main photovoltaic parameters for CoNi/MWCNT and Ni/MWCNT CEs are listed in tab. 3.4.1.

Sample	PCE (%)	J_{sc} (mA/cm^2)	V_{oc} (V)	FF (%)
Pristine MWCNTs	2.30	9.80	0.56	40
MWCNTs/Co-Ni ($N_{LP} = 10000$)	5.39	10.94	0.63	78.2
MWCNTs/Co-Ni ($N_{LP} = 20000$)	5.84	11.72	0.66	75.5
MWCNTs/Co -Ni ($N_{LP} = 30000$)	6.24	13.37	0.62	75.3
MWCNTs/Co-Ni ($N_{LP} = 40000$)	6.68	14.68	0.63	72.2
MWCNTs/Co-Ni ($N_{LP} = 50000$)	4.49	10.93	0.60	68.4
MWCNTs/Co-Ni ($N_{LP} = 60000$)	4.10	10.27	0.64	62.9
MWCNTs/Sputtered-Pt	6.22	13.36	0.59	78.9
MWCNTs/Ni ($N_{LP} = 5000$)	4.57	15.87	0.51	56.5
MWCNTs/Ni ($N_{LP} = 20000$)	6.11	14.94	0.64	63.9
MWCNTs/Ni ($N_{LP} = 40000$)	5.14	19.31	0.52	51.2
MWCNTs/Ni ($N_{LP} = 60000$)	4.77	13.07	0.59	61.9

As it is possible to see from fig. 3.12 and tab. 3.4.1, the decoration of

MWCNT with Ni or CoNi nanoparticles improved the photovoltaic properties of the devices with respect to the pristine MWCNT counter electrode. In particular, for the CoNi/MWCNT CEs the open circuit voltage (V_{oc}) ranges between 0.60 V to 0.66 V, and the short circuit current density (J_{sc}) ranges from 10.27 mA/cm^2 to 14.68 mA/cm^2 whereas for the Ni/MWCNT CEs the open circuit voltage ranges between 0.51 V to 0.64 V and the short circuit current density ranges from 13.07 mA/cm^2 to 19.31 mA/cm^2. These are reasonable values for DSSC devices as reported in [80, 81] exceeding those of pristine MWCNTs-based DSSC (for which V_{oc}0.56 V and J_{sc} = 9.8 mA/cm^2). Consequently, also the power conversion efficiency (PCE) of both the Ni/MWCNT and of the CoNi/MWCNT CEs shows a good increase with respect to the pristine MWCNT CEs, confirming the effectiveness of the PLD-decoration in enhancing the performance of the DSSC devices. Fig. 3.12 and tab. 3.4.1 evidence also that the photovoltaic performance depends on the number of laser pulses used during the PLD decoration process. To go deeper in details about the Ni/MWCNT CEs, the one decorated at N_{LP} = 20000 has J_{sc} = 14.94 mA/cm^2 and V_{oc} = 0.64 V which is also the highest obtained for these Ni-decorated CEs. The fill factor calculated for this device is FF = 63.9% and PCE = 6.11%. This PCE value is the highest obtained among all the other Ni/MWCNT CEs and the pristine MWCNT CEs (that reached only PCE = 2.30%). For the CoNi/MWCNT CEs, instead, the sample decorated at N_{LP} = 40000 showed the highest value of short circuit current density J_{sc} = 14.68 mA/cm^2) with a V_{oc} = 0.63 V and achieving consequently its PCE = 6.68% which is about 190% higher with respect to the PCE value obtained for the pristine MWCNTs CE based DSSC device.

For higher N_{LP}, however, the photovoltaic performance of the devices show a slight decrease, finally reaching for the Ni/MWCNT PCE = 4.77% with a V_{oc} = 0.59 V and a J_{sc} = 13.07 mA/cm^2. The CoNi/MWCNTs reached PCE = 4.10% with V_{oc} = 0.64 V and J_{sc} = 10.27 mA/cm^2. By comparing the results obtained for both the Ni/MWCNT and the CoNi/MWCNT decorated CEs with the standard Pt-sputtered CE is evident that only the CoNi/MWCNT decorated at N_{LP} = 40000 had an improvement with respect to the Pt-sputtered CE. The latter, in fact, had J_{sc} = 13.36 mA/cm^2 and a V_{oc} = 0.59 V that are both lower if compared with the values obtained for the N_{LP} = 40000 CoNi/MWCNT CE. Consequently, also the PCE of the Pt CE showed a value of 6.22% which is lower compared with the PCE of the N_{LP} = 40000 CoNi/MWCNT CE (PCE = 6.68%, which is about 7.8% higher than the PCE of Pt CE). Nevertheless, the fill factor calculated for the Pt CE was FF = 78.9% that is higher with respect to that of N_{LP} = 40000 CoNi/MWCNT CE (FF = 72.2%), but it didn't affect the performance of the DSSC device.

The higher photovoltaic properties of both Ni/MWCNT (N_{LP} = 20000) and CoNi/MWCNT (N_{LP} = 40000) with respect to the pristine MWCNT
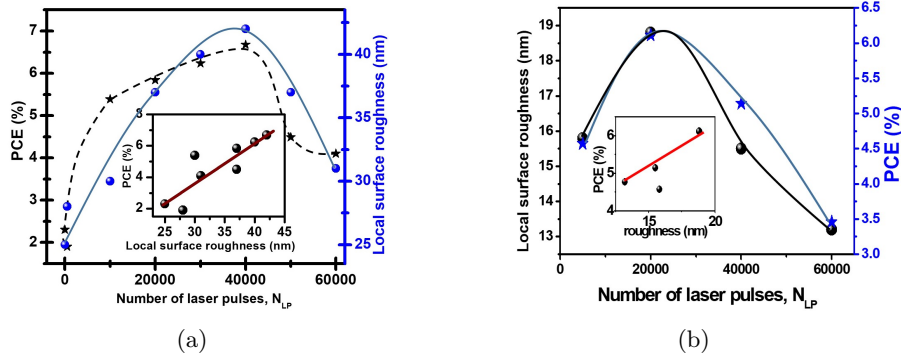
(a)
(b)

Figure 3.13: Plot of the power conversion efficiency (PCE) (black lines) and of the local surface roughness (blue lines) as a function of the number of laser pulses N_{LP} used to decorate the MWCNT counter electrode with (a) CoNi nanoparticles and (b) Ni nanoparticles. The insets show the linear correlation between the improved PCE of the different CEs and their respective local surface roughness.

CE, and also the improvement that the latter showed with respect to the platinum can be addressed to the direct correlation between the high surface roughness and the catalysis that takes place at the interface between the CE and the electrolyte solution. In fact, MWCNT, Pt, Ni and CoNi are all good catalysts but they differ in local surface roughness (the Pt has a roughness of about 10 nm, while the CoNi/MWCNT decorated at $N_{LP} = 40000$ has a roughness of 42 nm and the Ni/MWCNT decorated at $N_{LP} = 20000$ has a roughness of 18.8 nm). The strict correlation between the PCE and the local surface roughness (i.e. the N_{LP}) is showed in fig. 3.13. This is the first time that such a correlation has been observed over a wide surface roughness range.

Observing fig. 3.13 (a) and (b), first of all, it is important to notice that for the CoNi/MWCNTs CEs the PCE increases together with the local surface roughness for N_{LP} varying from 500 to 40000, while both tend to decrease for higher values of number of pulses ($N_{LP} = 50000 - 60000$). In particular, both the PCE and the roughness curves show a maximum in correspondence of the same number of laser pulses ($N_{LP} = 40000$). This particular behaviour confirms that the synergistic effect between the uniform coverage of the MWCNT by CoNi nanoparticles and the presence of the cauliflower-like structure of the nanoparticle layer improves the transfer of electrons from the CE to the electrolyte solution, boosting the PCE performance of the DSSC device. In fact, as already discussed inside the UPS section, the CoNi/MWCNTs counter electrode decorated at $N_{LP} = 40000$ shows the lowest work function value ($\Phi = 3.9$ eV) thus it has higher energy

electrons that ensure a superior catalytic activity in reducing the redox species, as reported in [82].

A further insight in the correlation between the roughness and the photovoltaic property of the DSSC device is given by the cross-plotting of the PCE calculated for the different CEs as a function of their local surface roughness, showed in the inset of fig. 3.13 (a). These two parameters, in fact are linearly correlated to each-other and this result highlights, once again, the key role played by the local surface roughness in enhancing the PCE of the DSSC device. Moreover, it is the first time that a direct linear correlation between these two parameter was experimentally confirmed over a wide surface roughness range. The use of PLD to decorate MWCNTs with metal nanoparticles, thus, is demonstrated to be an effective and fast method to obtain tailored features on the substrate surface, guaranteeing a fine tune on the morphological properties of the material. The enhancement of the PCE with respect to the standard Pt CE observed for the CoNi/MWCNTs CE highlights also the possibility to replace the expensive platinum with low-cost materials and, at the same time, even improve the photovoltaic performance of the device, which is a critical step forward in the direction of a future commercialization of DSSC devices on a large scale production.

Chapter 4

Working Electrodes in DSSCs

The Working Electrode (WE) or photoanode is responsible of the most important process that takes place inside the dye-sensitized solar cells. The dye molecules are readily excited by the incident light radiation and the result of this excitation process is the production of photoelectrons. The TiO_2 enables the transport of these photo-generated electrons from the dye molecules to the conductive glass substrate. However, the secondary processes (such as the electron/hole recombination process, or the decay of photoelectron inside the dye molecules themselves) that take place in the working electrode are responsible for the low efficiency achieved by this solar cell device and are the major obstacle to the entry of DSSC in the solar technology market.

Our approach was thus focused on the enhancement of the charge transport inside the TiO_2 layer, trying to limit if not completely avoid the secondary processes that occur inside the working electrode.

4.1 Effects of the addition of weighted amount of CNT to the TiO_2 thin film

The addition of carbon nanotubes in the TiO_2 thin film, as already discussed in the State of art section, plays an important role in the reduction of the optical band gap of the semiconductor material, determining also a shift of the maximum of light absorption toward the visible region of the spectrum [35, 39, 45] Moreover, several studies confirmed that the presence of this carbon-based nanomaterial greatly enhances the photovoltaic properties of the DSSC devices if added in low weighted percentages compared to the amount of TiO_2 [83, 84]. Adding high amounts of CNT to TiO_2 was revealed to determine a dramatic loss of efficiency [41, 44].

During my experimental studies I deeply investigated this particular
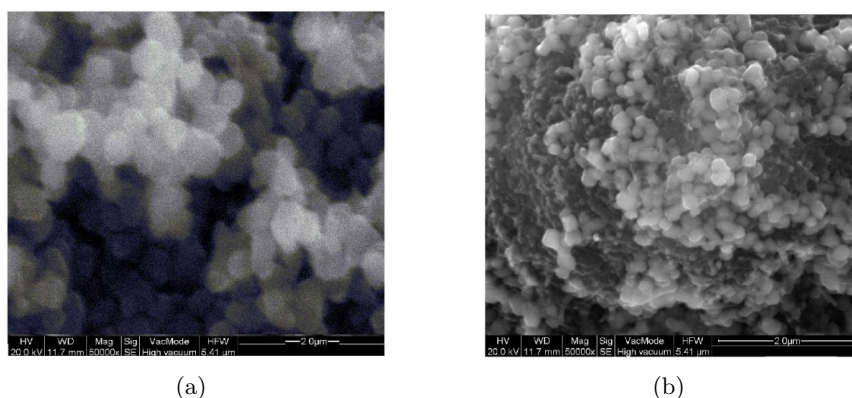
(a)   (b)

Figure 4.1: SEM images of CNT/TiO2 hybrid films with different wt.% of CNT: CNT (0.5 wt.%)/TiO$_2$, and CNT (5 wt.%)/TiO$_2$.

behaviour of the CNT-doped TiO_2 photoanodes finding a strict correlation between the loss of efficiency and the different morphologies of the samples determined by the amount of CNT used. The TiO_2 used for the photoanode preparation is a commercial powder purchased from Advanced Materials (average grains dimension 200nm), the MWCNTs are also a commercial powder of bundles purchased from Nano-lab co. USA with a nominal purity > 95%, average diameter of about 20-30 nm and average length of about 10μm. The pristine TiO_2 paste and the $CNT - TiO_2$ paste where prepared following the standard procedure reported in [44]. First of all, 0.2g of TiO_2 were dispersed in 0.4 mL of acetic acid, obtaining a uniform suspension. In order to obtain a uniform paste, 15.52 μL of acetylacetone, 0.4 mL of PEG2000 aqueous solution and 3.24 μL of Triton X-100 were added to the TiO_2 suspension. The $CNT - TiO_2$ paste was prepared following the same procedure, by adding weighted percentages of MWCNT powder (from 0.1% to 5% of the TiO_2 weight) to the TiO_2 powder. The pristine TiO_2 paste and the different $CNT - TiO_2$ pastes were then deposited on FTO glasses by using a spin coater and heated in air at 400 °C for 30 minutes in order to favour the solvent evaporation. Finally, 80 μL of Cis-Bis(isothiocyanato)Bis(2,2'-bipyridyl-4,4'-dicarboxylato) ruthenium (II) dye (N719 dye) were deposited on each photoanode. To obtain the dye desorption from the TiO_2 and from the $CNT - TiO_2$, the photoanodes were immersed in 40 mL of a solution 0.1 M of NaOH in EtOH/H$_2$O. To quantify the amount of dye molecules desorbed from the photoanodes, the absorbance spectra was acquired for each colloidal solution following the procedure described in [85]. As it is showed in SEM images (fig. 4.1), for low concentration the CNTs are randomly distributed among the TiO$_2$ grains, whereas for higher concentrations, the film appears inhomogeneous, as made of aggregates of CNTs randomly inserted among the TiO$_2$ grains.
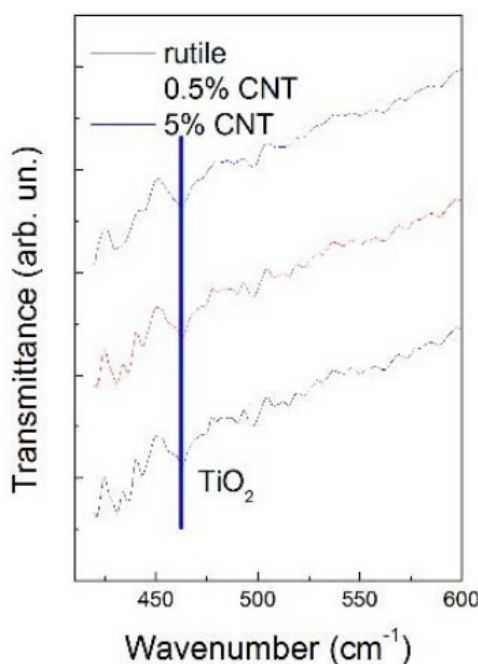
Figure 4.2: FTIR spectra taken on pure rutile, CNT (0.5wt.%)/rutile, and CNT (5 wt.%)/rutile.

As expected by looking at the film morphology, the interaction between CNTs and TiO$_2$ grains is only due to Van der Waals forces, while any other chemical bond between these two materials is absent. the FTIR spectra (fig. 4.2), infact, presents only the typical band of rutile phase centred at $471 cm^{-1}$ [86, 87]. Moreover, XPS measurements were already conducted on the same material in a previous work [43], confirming the absence of chemical bonds between the rutile and the carbon nanotubes.

The morphology of the film plays a key-role in the dye absorption process. The extinction cross section measured for the dye desorbed from film with high amount of CNTs (5%) is about 70% lower than that measured for a film of pure TiO_2 as showed in fig. 4.3.

In fig. 4.4 is showed the gaussian analysis of the extintion cross section for pristine TiO_2 (panel a) and of 5 wt.% $CNT - TiO_2$ (panel b). For the pure TiO_2 it is clearly visible the presence of two plasmonic structures centred at 518 nm and 580 nm that are typical of the absorption of particles of about 30-50 nm of diameter, as estimated by using the electrodynamic Mie-Gans theory. The difference of nanoparticle's dimension between the observed signals and the data specified in the datasheet of TiO_2 is due to the sonication process used to disperse the nanoparticle: the sonication process in fact determined the de-aggregation of the 200 nm granis in to smaller nanoparticles. For the $CNT - TiO_2$, instead, the plasmonic peaks
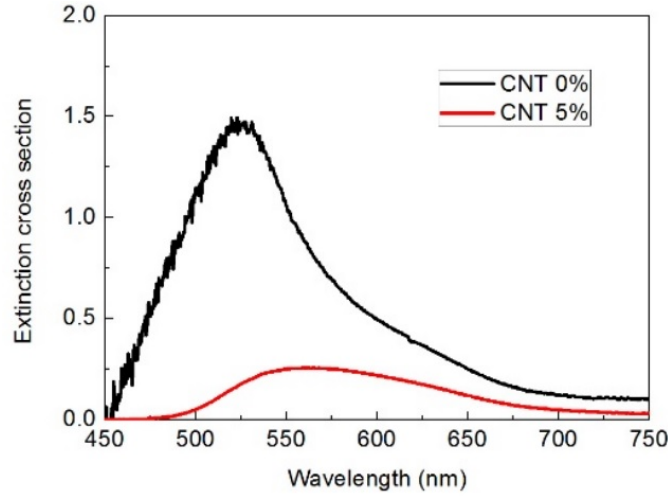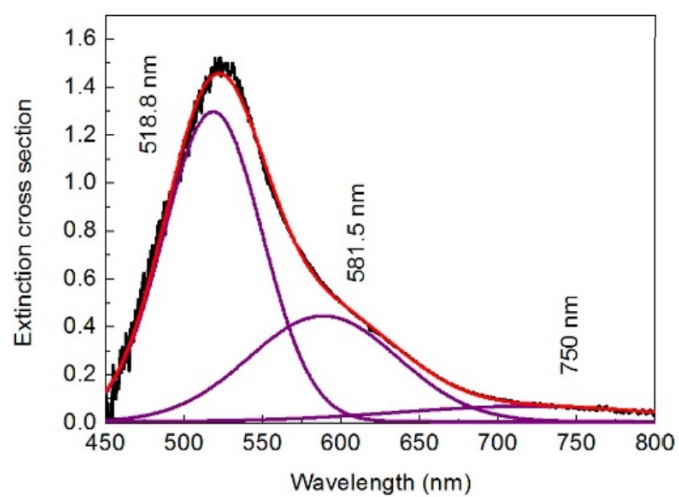
Figure 4.3: Extinction cross sections for the desorbed dye from $CNT - TiO_2$ film with 5% (red curve) of CNT and for the pristine TiO_2 (black curve). The former curve is about 70% lower than the latter indicating the CNTs play a key role in the absorption of the dye molecules.

present a red-shift, with peaks located at 540 nm and 600 nm that are typical of the absorption of particles with diameters ranging between 40 nm and 70 nm. The presence of high amount of CNTs inside the TiO_2 film, then, could have reduced the fine porosity of the film, eventually forming also big aggregates of CNT and thus reducing the absorption properties of the TiO_2 film. The disappearance of small pores of the material was confirmed also by the roughness measurement conducted via AFM on both the pure TiO_2 film (fig. 4.5 panel a) and the 0.5 wt.% $CNT - TiO_2$ film (fig. 4.5 panel b). the former showed a roughness of about 41 nm while the latter shows a roughness of 51 nm, with an increase of about 25% with respect to the pristine TiO_2 film. The presence of the CNT aggregates inhibits the dye absorption from rutile. For CNT amount greater than 0.5 wt.%, instead, the film appears as composed of different and well separated areas of TiO_2 grains and of CNT aggregates.

The roughness evaluation conducted in those areas evidenced, as expected, the value of 41 nm in the TiO_2 areas (in accordance with the measurement conducted on the pure TiO_2 film), and the value of 120 nm in the CNT areas (that is indeed typical of carbon nanotubes bundles). The dye absorption in these non-uniform film, then, is affected by the presence of these well-separated areas since they interact differently with the dye molecules: the large CNT areas with high roughness is responsible of a reduction of the dye absorption, causing consequently also a loss in the photovoltaic performance of the solar cell. The efficiency, in fact, increases of about the 5% for the 0.5 wt.% $CNT - TiO_2$ photoanode, but shows a loss of about the 10% when

(a)
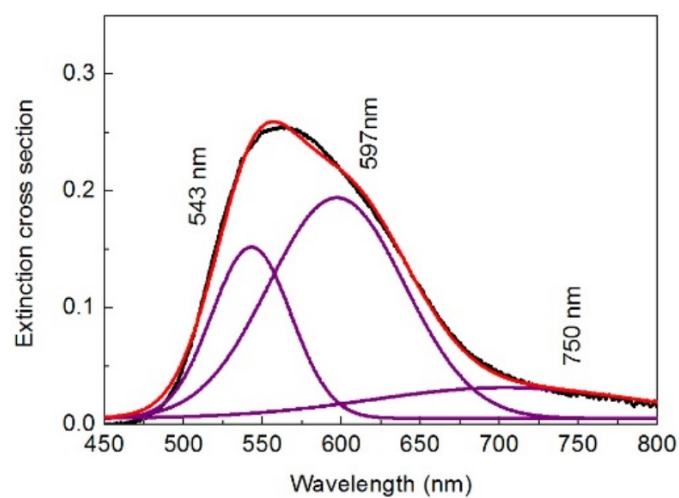
(b)

Figure 4.4: Gaussian analysis of the extinction cross section for pristine TiO_2 (a) and for 5 wt.% $CNT - TiO_2$ (b)
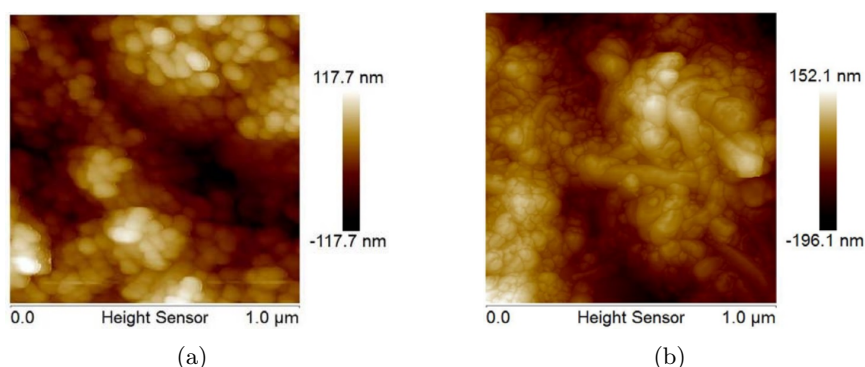
Figure 4.5: AFM images of pristine TiO_2 film (a) and of $0.5wt.\%CNT-TiO_2$ film

using the 1 wt.% $CNT-TiO_2$ photoanode. The total amount of adsorbed dye molecules, in fact, decreases exponentially with the increase of CNT amount added to the TiO_2 film, as showed in fig. 4.6.

It confirms once again that the addition of CNT to the TiO_2 thin film is strongly effective only for low wt.% of CNT (0.5 wt.% in our case) since it ensure the best balance between the improvement of the optical properties of the photoanode (a quench of the photoluminescence intensity of about 20% and a reduction of the optical band of about 1.5 %) and the loss of dye absorption (that is "only" of about 20%).

4.2 Effects of the addition of weighted amount of G to the TiO$_2$ thin film

Graphene is another very promising carbon-based nanomaterial that can be added to the TiO_2 thin film to enhance the photovoltaic performance of the photoanode, as reported in the State of art section. However, as pointed out before, the interaction between this nanomaterial and the dye absorption in the TiO_2 thin film is still not clear. To explore the overall effects of the doping with graphene on the photoanode, different weighted amounts of this carbon-based nanomaterial (ranging from from 0.05 wt.% to 1 wt.%) were added to the TiO_2 film following the same procedure previously used for the preparation of the $CNT-TiO_2$ photoanodes [88]. All the photoanodes where then bathed in N719 dye for 24 hours, rinsed with ethanol to remove the excess of dye and dried in air.

These different photoanodes were then characterized to assess the effects of graphene on the photovoltaic properties and to the dye absorption. At first, to ensure the absence of impurities on the photoanodes, the Energy Dispersive X-Ray Spectrometry (EDS) was performed on all the G-doped
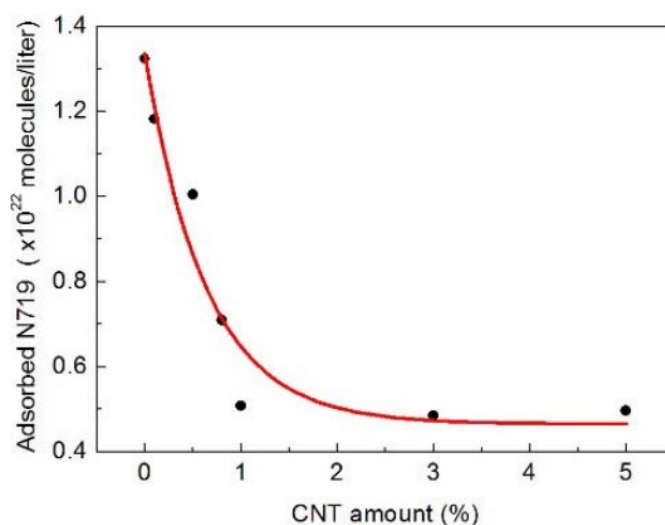
57

Figure 4.6: Dye desorption as function of CNT weighted amount

TiO_2 film. In fig. 4.7 is reported the EDS spectra of dye-sensitized 0.1 wt.% $G - TiO_2$ photoanode as example for all the samples. The spectra show a strong signal of Ti and of O as predominant element of the film, that are present in a percentage of 26.89% and 57.46%, respectively. The photoanodes composition presents also traces of C (15.48%) due to the graphene, and of Ru (0.17%), due to the N719 dye molecules used to sensitize the photoanodes. The absence of other peaks confirmed the absence of impurities.

The morphologies of the pristine TiO_2 film and of the $G - TiO_2$ photoanodes were investigated by using a SEM microscope (fig. 4.8).

The pristine TiO_2 photoanode (fig. 4.8 panel a) consists of a uniform film of TiO_2 nanograins, with absence of noticeable features on its surface. The surface appears to have small pores without the formation of aggregates of TiO_2 particles. The morphology of the photoanodes doped with different weighted percentages of graphene is showed in fig. 4.8 panels b and c. Since the amount of graphene added into the TiO_2 film is very low, and since the graphene is also well dispersed between the grains, it is impossible to observe the graphene sheets by these SEM images. The presence of graphene is, however, confirmed by the EDS spectra showed before. Comparing fig. 4.8 b and c, it is not possible to notice visible changes in the samples' morphology with the increase of the amount of graphene used in the TiO_2 photoanode.

The addition of graphene to the TiO_2 film, however, enhances the photovoltaic properties of the photoanode. Its high conductivity in fact improves the transport of photo-generated electrons from the TiO_2 to the FTO-glass avoiding the electron/hole recombination that usually occurs inside the undoped TiO_2 film. The reduction of the recombination process causes an improvement in the photovoltaic performance of the G-doped photoanodes
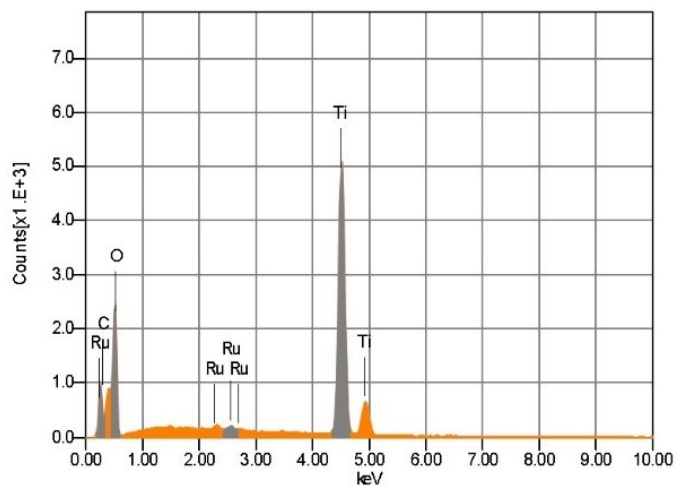
Figure 4.7: EDS spectra of dye-sensitized 0.1 wt.% $G - TiO_2$ photoanode
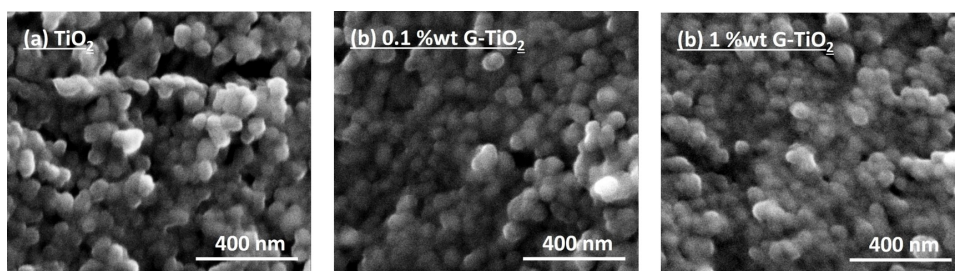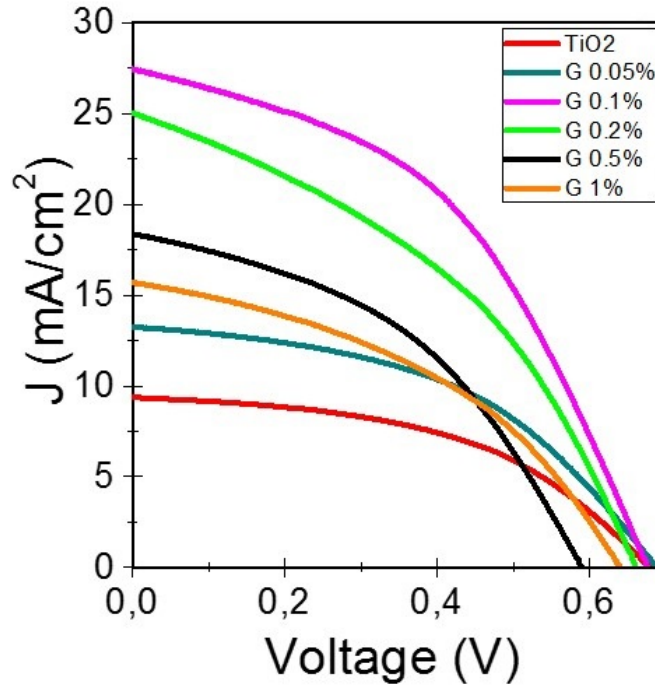

Figure 4.8: Top view SEM images of: (a) pure TiO2, (b) 0.1 wt% G-TiO2, (c) 1 wt% G-TiO2 photoanodes

Figure 4.9: J-V curves for pure TiO_2 and graphene-doped TiO_2

compared to the pristine TiO_2. The J-V curves showed in fig. 4.9 were all acquired under solar simulator operating in the standard condition (1.5 AM and $P = 100mW/cm^2$), while the photovoltaic parameters are listed in table 4.1. The pristine TiO_2 and all the G-doped TiO_2 photoanodes were assembled together with a standard Pt counter electrode.

As expected, all the $G - TiO_2$ photoanodes showed an increase of their phovoltaic performances if compared with that of the pristine TiO_2 photoanode. In particular, the V_{oc} ranges from 0.59 V for $0.5wt.\%G - TiO_2$ to 0.69 V for $0.05wt.\%G - TiO_2$, whereas the J_{sc} showed values varying from

	$J_{SC}(mA/cm^2)$	$V_{OC}(V)$	$PCE(\%)$	$FF(\%)$
TiO_2	9.30+-0.02	0.68+-0.02	3.0+-0.1	47.6+-0.1
$0.05wt.\%G - TiO_2$	13.16	0.69	4.2	46.4
$0.1wt.\%G - TiO_2$	27.49	0.67	8.2	44.7
$0.2wt.\%G - TiO_2$	24.99	0.66	6.4	38.7
$0.5wt.\%G - TiO_2$	18.70	0.59	4.6	41.2
$1wt.\%G - TiO_2$	15.58	0.64	4.2	41.8

Table 4.1: photovoltaic parameters of DSSC assembled by varying the amount of graphene in the TiO_2 film
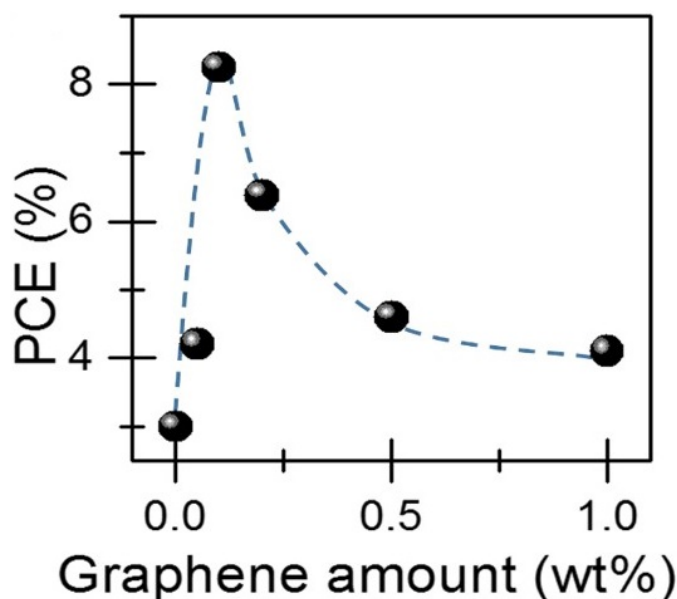
Figure 4.10: trend of the PCE values as a function of the graphene weight amount used to dope the the TiO_2 film.

13.16 mA/cm^2 at $0.05wt.\%G - TiO_2$, to 27.49 mA/cm^2 at $0.1wt.\%G - TiO_2$. Interestingly, the G-doped photoanodes showed a behaviour similar to the one already observed for the CNT: the power conversion efficiency (PCE) tends to increase only for low amount of graphene used, with a clear drop in its performance when the amount of graphene exceeds a certain value. The plot of PCE vs wt.% of graphene (fig. 4.10) shows a rapid increase of the PCE from the 3% of pristine TiO_2 to 8.2% for the $0.1wt.\%G - TiO_2$ photoanode. A further increase of the weighted percentage of graphene added to the TiO_2 film causes a decrease in the efficiency of the DSSC device from 6.4% at $0.2wt.\%G - TiO_2$ to 4.2% at $1wt.\%G - TiO_2$.

This drop of photovoltaic performances can be addressed to a different dye absorption of the G-doped photoanodes compared to the pristine TiO_2 film. The systematic characterization of the dye adsorption properties conducted on all the $G - TiO_2$ photoanodes by using the thermogravimetric analysis (TGA) confirmed this hypothesis. In fig. 4.11 are reported the thermogravimetric curve (TG - black), its derivative (DTG - red) and the Differential Scanning Calorimetry (DSC) for the $0.1wt.\%G - TiO_2$ photoanode sensitized with 1 mM of N719 dye, as example for all the photoanodes.

To generate the TG curve, the sample was heated at a constant heat rate of 5°C/min under an air flow of 50 cc/min by using a NETSCH instrument. Each step in the TG curve represent a loss in the sample's mass due to the destruction of the dye molecules and thus permits to quantify the amount of dye that was absorbed on the $G - TiO_2$ photoanode. From the TG curve of
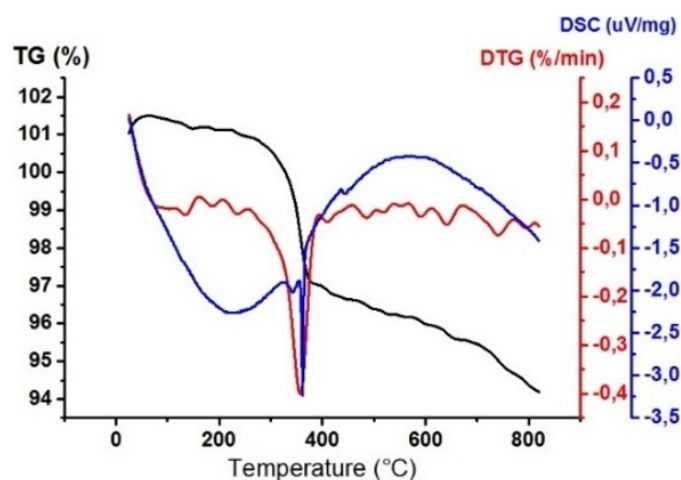
Figure 4.11: TG (black), DTG (red) and DSC (blue) curves of $0.1wt.\%G - TiO_2$ as example for all the $G - TiO_2$ composites.

fig. 4.11 it is immediately possible to identify two steps, the first is located in the 70°C-100°C range due to the endothermic dehydration process that causes the water evaporation from the $G - TiO_2$ porous film. The second step is quite deep and it is located in the 300°C-400°C range, representing the decomposition of the dye molecules. The derivative of the TG curve (DTG, represented by the red curve in fig. 4.11) permits to determine more precisely the terperature at whic the decomposition process of the dye molecule takes place. Infact, the DTG curve presents an intense and sharp peak located at about 357°C that is due to a decarboxylation reaction. To have a deeper insight in the decomposition process of the dye molecule, it is useful to use the DSC curve (blue curve in fig. 4.11). From this curve, in fact, it is possible to identify the sequential decomposition of the N719 dye molecules: the decarboxylation process starts at about 340°C [89], causing the transformation of the bipyridine ligands of N719 dye in CO_2. This decarboxylation process is then followed by a decomposition of the residuals organic components of the dye, ending when the temperature reaches about 380°C. The amounts of dye absorbed in each photoanode evaluated using this technique are listed in table 4.2.

The influence that the amount of graphene used has on the dye absorption and the consequent effect that the quantity of dye inside the film has on the efficiency of the DSSC solar cell is well represented in fig. 4.12.

By overlapping the trend of mass loss with the trend of PCE, it is clear that the amount of dye inside the photoanode remains almost constant when no to low amounts of graphene are added to the TiO_2 film but it decreases rapidly for graphene weighted percentages greater than 0.1 wt%. Similarly, the trend of PCE shows an increase of efficiency for low amounts

Sample	Mass loss (%) $\pm$ 0.02
TiO_2	3.54
$0.05wt.\%G - TiO_2$	3.56
$0.1wt.\%G - TiO_2$	3.52
$0.2wt.\%G - TiO_2$	2.82
$0.5wt.\%G - TiO_2$	2.78
$1wt.\%G - TiO_2$	2.58

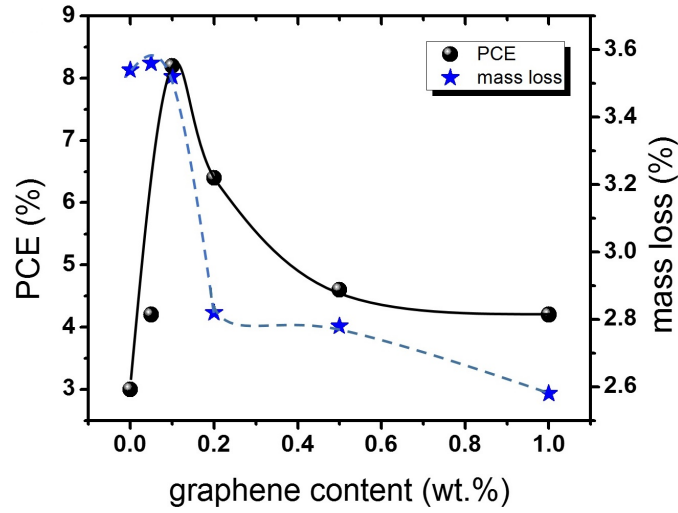Table 4.2: Amount of dye absorbed in the TiO_2 and $G - TiO_2$ thin films evaluated via TGA measurements.

Figure 4.12: Trend of PCE values and of percentage of weight loss as a function of graphene amount.
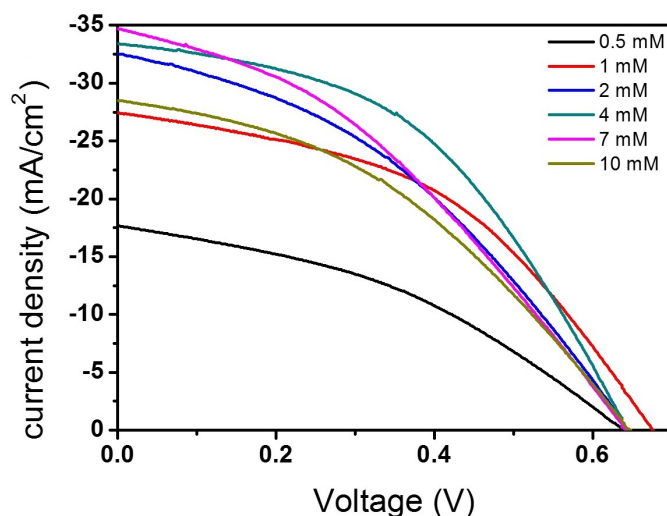
Figure 4.13: J-V curves for $0.1wt.\%G - TiO_2$ sensitized with different dye concentrations

of graphene added to the TiO_2, while for grapehene contents that exceed the 0.1 wt% it decreases. This similarity in the two trends can be addressed to a competition phenomenon between the graphene and the dye molecules in light harvesting [47]. The optimum in the doping of TiO_2 by using this particular 2D carbon-based nanomaterial is then reached for 0.1 wt.% of graphene. This quantity of grapehene used, in fact, does not affect negatively the dye absorption of the photoanode, while reducing the electron-hole recombination process that takes place inside the TiO_2 thin film. The influence that the amount of dye absorbed in the TiO_2 has on the overall photovoltaic performance of the photoanode was further investigated by bathing several optimized $0.1wt.\%G - TiO_2$ photoanodes into different dye solutions with concentration ranging from 1 mM to 10 mM. these sensitized photoanodes were then assembled in DSSC devices and their photovoltaic properties were measured under solar simulator. Fig.4.13 shows the J-V curves acquired for these $0.1wt.\%G - TiO_2$ photoanodes bathed in different dye concentrations. The photovoltaic parameters are listed in table 4.3

From the J-V curves it is possible to see that the photovoltaic performance of the DSSCs is influenced by the dye concentration used during the sensitization of the photoanodes. The efficiency of the DSSC increases together with the increase of the dye concentration, reaching a maximum for the photoanode sensitized with a 4mM dye solution. The use of dye solution with higher concentration, however, was demonstrate to have a negative influence on the photovoltaic performance of the DSSC: the efficiency for the photoanodes sensitized with higher dye concentration decreased to 8.1% (dye solution concentration of 7 mM) and 7.3% (dye solution concentration

	$J_{SC}(mA/cm^2)$ ±0.01	$V_{OC}(V)$ ±0.01	$PCE(\%)$ ±0.1	$FF(\%)$ ±0.1
0.5 mM	17.65	0.64	4.3	38.1
1 mM	27.49	0.67	8.2	44.7
2 mM	32.47	0.65	8.5	40.2
4 mM	33.37	0.64	9.5	44.6
7 mM	34.68	0.64	8.1	36.6
10 mM	28.41	0.64	7.3	40.0

Table 4.3: Photovoltaic parameters of DSSC loaded with different N719 dye concentrations.
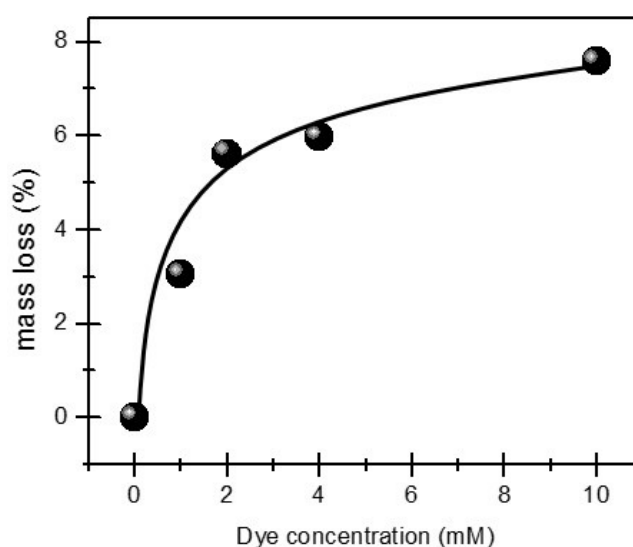

Figure 4.14: Saturation curve of the quantity of dye absorbed in $0.1wt.\%G - TiO_2$ photoanode (evaluated via TGA measurement) as a function of the dye concentration.

of 10 mM).

A good absorption of dye in the TiO_2 film is extremely important since it guarantees a high light harvest inside the photoanode. Thus, the different photovoltaic performances achieved with the different dye solution concentration can be addressed to a different absorption of dye inside the TiO_2 film. To measure the absorbed dye quantity a TGA analysis was performed for the photoanodes bathed in the different dye concentration solutions. Fig. 4.14 shows the trend of the mass loss as a function of the dye concentration, while the value obtained from the TGA analysis are listed in tab.4.4.

As general behaviour, from fig. 4.14 is clear that the percentage of absorbed dye inside the $0.1wt.\%G - TiO_2$ photoanodes increases with the dye concentration, passing from the 3.04% for the 1mM dye solution to

Sample	Mass loss (%) $\pm$ 0.02
1 mM	3.04
2 mM	5.62
4mM	5.97
10 mM	7.58

Table 4.4: amount of dye absorbed in the $0.1wt.\%G - TiO_2$ thin films evaluated via TGA measurements

the 5.97% of the 4mM dye solution. The curve tends to saturate for dye concentrations higher than 4 mM, slowly reaching a dye uptake of 7.58% for the 10 mM dye solution. A further insight in the photovoltaic behaviour of the photoanodes sensitized with different dye concentration was obtained by plotting the PCE as a function of the dye concentration (fig. 4.15)

From fig.4.15 it is evident that both the PCE and the dye uptake in the photoanodes have the same trend. The quantity of dye absorbed in the $G - TiO_2$ seems to be directly linked to the photovoltaic performances of the DSSC. In the inset of fig.4.15, in fact, it is showed the plot of PCE as a function of the amount of absorbed dye and it is possible to observe that the PCE reaches the highest value of 9.5% in correspondence of an amount of 5.97% of dye absorbed inside the photoanode, which is the dye uptake obtained from the 4mM dye solution. For higher dye amounts, the photovoltaic performances decrease to 7.3% of PCE, for a dye uptake of 7.58% inside the $G - TiO_2$ photoanode. This drop of efficiency of the solar cells when the photoanode is bathed in the dye solutions at concentration > 4 mM, can be explained considering that for concentration $\pm$ 4mM the quantity of dye absorbed inside the $G - TiO_2$ thin film saturates. Probably, the quantity of dye molecules around the TiO_2 grains is high enough to favour the decay of the photo-excited electrons from the HOMO to the LUMO levels of the dye molecules themselves, rather than the decay in the conduction band of TiO_2. this results underlines the existence of a maximum load of dye in the TiO_2 photoanode, in agreement with recent works [90, 91].

To conclude this Ph.D. project, I assembled the first prototype of a novel DSSC in which both the photoanode and the cathode are made with the newly developed $0.1wt.\%G - TiO_2$ WE and the $CoNi/MWCNT$ ($N_{LP} = 40000$) CE discussed in the previous chapter. The photoanode was sensitized with a 4mM N719 dye solution. In fig.4.16 is reported the very promising, although preliminary, photovoltaic performance obtained for this prototype. The PCE obtained by this device under solar simulator (AM 1.5, P=$100mW/cm^2$), in fact, is as high as 9.8% and could lead to further improving in the near future: more systematic work are needed to obtain a full optimization of this novel DSSC prototype.

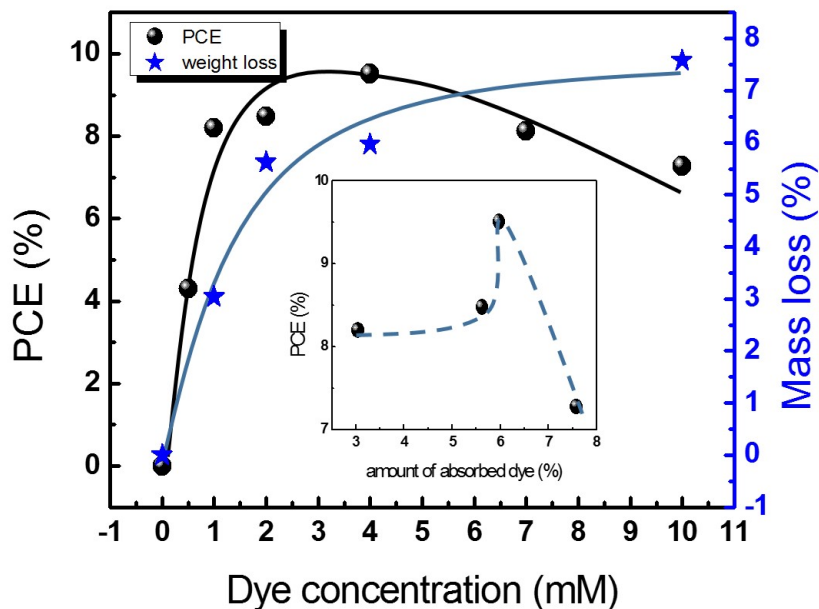Figure 4.15: Trend of both PCE and mass loss as function of dye concentration. Inset shows the trend of PCE as a function of the amount of absorbed dye, evidencing the presence of an optimal quantity of dye that strongly improves the PV property of the device.
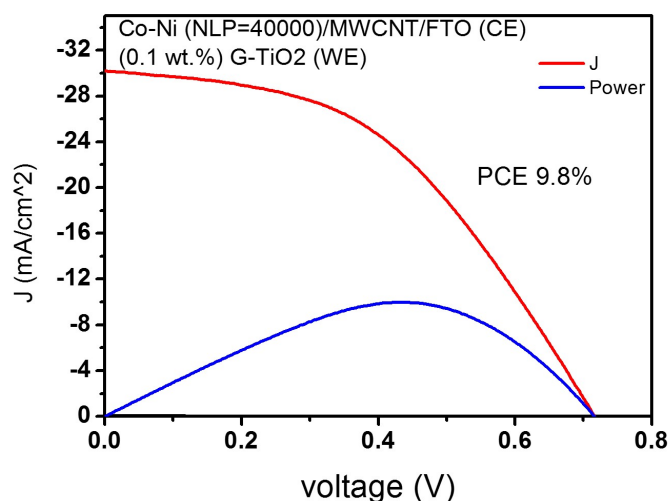

Figure 4.16: J-V curve of the novel DSSC assembled using $0.1wt.\%G - TiO_2$ as a photoanode and $CoNi/MWCNT$ ($N_{LP} = 40000$) as a cathode.

Conclusions and Future Perspectives

The aim of this Ph.D. project is to move toward the development of enhanced dye sensitized solar cells and their industrialization by using new materials that are less expensive though high performing in generating renewable energy.

The experimental line followed during the previous chapters demonstrated the possibility to improve the materials currently used to build the photoanode and the cathode in the DSSC devices. The general performance enhancement was obtained by using novel approaches during the preparation of those materials and by studying their role in the various processes that take place inside the DSSC and that allow the conversion of light into electrical energy.

The main results achieved during this Ph.D. project can be summarized as follows:

- This work shows a new easy and "green" way to decorate MWCNT with Ni or CoNi nanoparticles which dimensions and coverage can be accurately chosen via the PLD technique. The as-obtained counter electrodes were introduced inside DSSC devices and optimized by varying the N_{LP}, in order to achieve high photovoltaic performances. The variation of N_{LP} used during the PLD deposition grants a direct control over both the particle size distribution and the surface coverage rate of these metal or alloy nanoparticles on to the MWCNTs.

  It is worth noting that the aggregation of Ni or CoNi nanoparticles in a peculiar cauliflower-like structure at $N_{LP} = 40000$ grants a good local surface roughness of about 42 nm that boosts the photovoltaic performance of the DSSC, obtaining for the first time a $PCE = 6.68\%$ that is higher if compared to the pristine MWCNT and the standard Pt-based counter electrodes. The synergistic effects of the good local surface roughness and the well aligned global work function of CoNi-decorated MWCNTs with the FTO, in fact, enhances the catalysis reaction that takes place at the interface between the counter electrode and the electrolyte solution, causing as a consequence a great improvement in the power conversion efficiency of the solar cell. The direct correlation between the PCE and the local surface roughness, underlines the importance of using a PLD-based approach for the

decoration of MWCNT. In fact, it ensures a strict control over the morphological properties of the material and also allows to easily introduce inexpensive transition metal or alloy nanoparticles to replace the platinum as a counter electrode, even enhancing the performance of the DSSC.

- This work presents, for the first time, a possible explanation regarding the negative effects that the addition of an excessive amount of carbon-based materials (as carbon nanotubes (CNT) or graphene (G)) in the TiO_2 film could have on the performance of the DSSC.

Different weighted amounts of MWCNT and of G were added to the TiO_2 film, and their propriety were fully investigate finally finding the relationship between the amount of carbon-based material used and the dye absorption properties of the TiO_2 film. The addition of low wt.% of CNT or G to the TiO_2 efficiently improves the photocharge transport inside the photoanode, limiting the electron/hole recombination phenomenon and boosting the photovoltaic performance of the solar cells. On the other hand, the addition of excessive amounts of carbon-based materials has been demonstrated to seriously affect the absorption of dye in the TiO_2 film, causing a drop in the power conversion efficiency of these photoanodes. In particular, the addition of a quantity of MWCNT $> 0.5\%$ causes a progressive formation of big aggregates of carbon nanotubes in the TiO_2 film that cover the fine porosity of the film itself, with the consequent dramatic loss of its dye adsorption capability. The total amount of adsorbed dye molecules has been found to decreases exponentially with the increase of CNT amount, affecting negatively the photovoltaic performance of the DSSC. For MWCNT $> 0.5\%$, in fact, the solar cell registers a loss of 10% of PCE with respect to the standard solar cell while for $MCNT = 0.5\%$ the PCE has an increase of 5% with respect to the standard DSSC.

Similarly, also the addition of an excessive amount of graphene in the TiO_2 film causes a loss of dye absorption inside the photoanode with a consequent decrease of the photovoltaic performance. The overlap of the trend of the PCE and the trend of mass loss both as function of graphene amount, in fact, pointed out that both trends tend to decrease for graphene amount that exceeds the 0.1 wt.%. this particular behaviour may be due to a change in the morphology of the sample as the presence of an excessive quantity of graphene limits the absorption of dye in the TiO_2 film and thus affects negatively the photovoltaic performance of the photoanode. The impact of dye absorption on the PCE was confirmed by performing J-V measurements on several $0.1wt.\%G - TiO_2$ photoanode by varying the dye concentration used. For dye concentrations higher than 4 mM the percentage of dye absorbed inside

the $G-TiO_2$ film tends to saturate, while the PCE tends to decrease. This loss of photovoltaic performance can be addressed to competitive phenomena in light harvesting between the graphene and the dye molecules. It was then possible to find an optimum load of graphene and also an optimum dye concentration to boost the photovoltaic properties of the photoanode, with the aim to make them more efficient and competitive for future industrialization.

To conclude this Ph.D. project and to have a first insight on the future prospectives of this work, a completely novel DSSC was assembled. The novel solar cell consists of the CoNi/MWCNT counter electrode decorated at $N_{LP} = 40000$ and of the $0.1wt.\%G-TiO_2$ that are the most promising electrodes developed during this work. Moreover, the photoanode was sensitized by using 4 mM N719 dye solution which was demonstrate to be the best solution concentration for this particular dye. The as-assembled novel DSSC showed very promising photovoltaic performances, reaching a PCE value of about 9.8%. This high value of PCE is the result of the synergistic effect of the good catalysis (obtained by replacing the platinum in the counter electrode with the CoNi-decorated MWCNT that is a novel and more catalytic material), and the damped electron/hole recombination process (obtained by introducing the graphene as conductive material in the TiO_2 film in the working electrode, enhancing the charge transport). Moreover, the sensitization of the photoanode by using a particular concentration of dye solution ensured to have enough dye molecules in the photoanode to produce high amounts of photoelectons and, at the same time, to avoid the problem of their decay in the levels of the dye molecules itself (problem that usually occurs when an excessive amount of dye is absorbed in the TiO_2 film).

A further step on the study of these novel DSSC devices will be the study of their stability over time, by exposing them under the solar simulator for several weeks and comparing the time variation of the PCE of these novel DSSC with that of the standard DSSC. The stability of the photovoltaic efficiency over time is a crucial parameter in the introduction of novel solar cells device on the photovoltaic technology market.

Appendix

4.3 List of publication

- A. Imbrogno, A. Macario, M. Barberio, R. Pandiyan, A. Bonanno, and M. A. El Khakani, Effect of Graphene Doping in DSSC TiO_2 Photoanode. Advanced Science Letters 23(6) (2017) 5931-5933

- A. Imbrogno, R. Pandiyan, M. Barberio, A. Macario, A. Bonanno, M. A. El Khakani, Pulsed-laser-ablation based nanodecoration of multi-wall-carbon nanotubes by Co-Ni nanoparticles for dye-sensitized solar cell counter electrode applications, Mater. Renew. Sustain. Energy (2017) 6: 11

- M. Barberio, D.R. Grosso, A. Imbrogno, F. Xu, Preparation and photovoltaic properties of layered TiO_2/carbon nanotube/TiO_2 photoanodes for dye-sensitized solar cells, Superlattices and Microstructures 91 (2016) 158-164

- M. Barberio, A. Imbrogno, A. Bonanno, F. Xu, Ruthenium Dye absorption properties of CNT/TiO_2 composites, Journal of Chemistry and Chemical Engineering 9 (2015) 245-252

- M. Barberio, A. Imbrogno, F. Stranges, A. Bonanno, F. Xu, Controlled Synthesis of ZnS quantum dots with cubic crystallinity by laser ablation in solution, Materials Research Express – IOP 2 (2015) 055008

- M. Barberio, A. Imbrogno, D. Grosso, A. Bonanno, F. Xu, Low-cost Carbon-based Counter Electrodes for Dye Sensitized Solar Cells, Mater. Res. Express 2 (2015) 075502

- M. Barberio, P. Barone, A. Imbrogno, F. Xu, CO2 adsorption on silver nanoparticles/carbon nanotubes nanocomposites: a study of absorption characteristic, Phys. Status Solidi B 252, No. 9 (2015) 1955–1959

4.4 Attendance to International conferences

4.4.1 International conferences proceeding

- M. Barberio, F. Stranges, A. Imbrogno, F. Xu, Growth of Core/Shell Quantum Dots/Titanium dioxide hybrid films, Surface & Coatings Technology (2015), pp. 259-264

- M. Barberio, S. Veltri, F. stranges, A. Imbrogno, A. Bonanno, P. Antici, TiO2 and SiO2 nanoparticles film for cultural heritage: conservation and consolidation of ceramic and stone artifacts, Surface & Coatings Technology (2015), pp. 174-18

4.4.2 National and international Congress Communications

- A. Imbrogno, R. Pandiyan, M. Barberio , A. Macario, A. Bonanno and M. A. El Khakani "Pulsed-laser-ablation based nanodecoration of multi-wall-carbon nanotubes by Co-Ni nanoparticles for dye-sensitized solar cell counter electrode applications" Plasma Quebec Conference Le plasma : de l'espace au laboratoire – Montreal, Canada, 2017. Poster session

- A. Imbrogno, A. Macario, M. Barberio, R. Paniyan, A. Bonanno, M. A. El Khakani "Effect of graphene doping in DSSC TiO2 photoanode" VI International Workshop on Oxide-based Materials: Perspectives in Material Science and Technological Applications – Naples, Italy, 2016. Poster session

- M. Barberio, P. Barone, F. Stranges, A. Imbrogno, F. Xu "Growth of Core/Shell Quantum Dots/Titanium dioxide hybrid films" Nanosmat Europe – Dublin, Ireland, 2014. Poster session

- M. Barberio, P.barone, A. Imbrogno, F. Xu "Optical Characterization of Carbon Nanotubes/TiO2 Nanocomposites" Nanosmat USA – Houston, Texas, 2014. Poster session

- M. Barberio, P.barone, A. Imbrogno, F. Xu "Preparation and Characterization of Nanocomposites Based on Carbon Nanotubes and Metal Nanoparticles" Nanosmat USA – Houston, Texas, 2014. Oral session

Bibliography

[1] E. Commission, "2020 climate & energy package." `https://ec.europa.eu/clima/policies/strategies/2020_en`, 2008. [Online; accessed 15-October-2017].

[2] E. Karakaya and P. Sriwannawit, "Barriers to the adoption of photovoltaic systems: The state of the art," *Renewable and Sustainable Energy Reviews*, vol. 49, pp. 60–66, 2015.

[3] R. King, D. Law, K. Edmondson, C. Fetzer, G. Kinsey, H. Yoon, R. Sherif, and N. Karam, "40% efficient metamorphic gainp/ gainas/ ge multijunction solar cells," *Applied physics letters*, vol. 90, no. 18, p. 183516, 2007.

[4] M. Pagliaro, G. Palmisano, R. Ciriminna, and V. Loddo, "Nanochemistry aspects of titania in dye-sensitized solar cells," *Energy & Environmental Science*, vol. 2, no. 8, pp. 838–844, 2009.

[5] N. S. Sariciftci, "Polymeric photovoltaic materials," *Current opinion in solid state and materials science*, vol. 4, no. 4, pp. 373–378, 1999.

[6] R. F. Service, "Solar energy. outlook brightens for plastic solar cells.," *Science (New York, NY)*, vol. 332, no. 6027, p. 293, 2011.

[7] B. O'Regan and M. Graetzel, "A low-cost, high-efficiency solar cell based on dye-sensitized colloidal TiO2 films," *Nature*, vol. 353, pp. 737–740, Oct. 1991.

[8] T. N. Murakami and M. Grätzel, "Counter electrodes for dsc: application of functional materials as catalysts," *Inorganica Chimica Acta*, vol. 361, no. 3, pp. 572–580, 2008.

[9] G. Calogero, P. Calandra, A. Irrera, A. Sinopoli, I. Citro, and G. Di Marco, "A new type of transparent and low cost counter-electrode based on platinum nanoparticles for dye-sensitized solar cells," *Energy & Environmental Science*, vol. 4, no. 5, pp. 1838–1844, 2011.

[10] X. Yin, Z. Xue, and B. Liu, "Electrophoretic deposition of pt nanoparticles on plastic substrates as counter electrode for flexible dye-sensitized solar cells," *Journal of Power Sources*, vol. 196, no. 4, pp. 2422–2426, 2011.

[11] P. Li, J. Wu, J. Lin, M. Huang, Z. Lan, and Q. Li, "Improvement of performance of dye-sensitized solar cells based on electrodeposited-platinum counter electrode," *Electrochimica Acta*, vol. 53, no. 12, pp. 4161–4166, 2008.

[12] E. Olsen, G. Hagen, and S. E. Lindquist, "Dissolution of platinum in methoxy propionitrile containing lii/i 2," *Solar Energy Materials and Solar Cells*, vol. 63, no. 3, pp. 267–273, 2000.

[13] D. R. Wilburn and D. I. Bleiwas, "Platinum-group metals—world supply and demand," *US geological survey open-file report*, vol. 1224, pp. 2004–1224, 2004.

[14] B.-K. Koo, D.-Y. Lee, H.-J. Kim, W.-J. Lee, J.-S. Song, and H.-J. Kim, "Seasoning effect of dye-sensitized solar cells with different counter electrodes," *Journal of Electroceramics*, vol. 17, no. 1, pp. 79–82, 2006.

[15] U. Mehmood, A. U. Rehman, H. M. Irshad, A. U. H. Khan, and A. Al-Ahmed, "Carbon/carbon nanocomposites as counter electrodes for platinum free dye-sensitized solar cells," *Organic Electronics*, vol. 35, pp. 128–135, 2016.

[16] P. Sharma and P. Ahuja, "Recent advances in carbon nanotube-based electronics," *Materials Research Bulletin*, vol. 43, no. 10, pp. 2517–2526, 2008.

[17] L.-M. Peng, Z. Zhang, and S. Wang, "Carbon nanotube electronics: recent advances," *Materials today*, vol. 17, no. 9, pp. 433–442, 2014.

[18] J. G. Nam, Y. J. Park, B. S. Kim, and J. S. Lee, "Enhancement of the efficiency of dye-sensitized solar cell by utilizing carbon nanotube counter electrode," *Scripta Materialia*, vol. 62, no. 3, pp. 148–150, 2010.

[19] W. J. Lee, E. Ramasamy, D. Y. Lee, and J. S. Song, "Efficient dye-sensitized solar cells with catalytic multiwall carbon nanotube counter electrodes," *ACS applied materials & interfaces*, vol. 1, no. 6, pp. 1145–1149, 2009.

[20] J. E. Trancik, S. C. Barton, and J. Hone, "Transparent and catalytic carbon nanotube films," *Nano Letters*, vol. 8, no. 4, pp. 982–987, 2008.

[21] S. Hwang, J. Moon, S. Lee, D.-H. Kim, D. Lee, W. Choi, and M. Jeo, "Carbon nanotubes as counter electrode for dye-sensitised solar cells," *Electronics Letters*, vol. 43, no. 25, pp. 1455–1456, 2007.

[22] K.-C. Huang, Y.-C. Wang, R.-X. Dong, W.-C. Tsai, K.-W. Tsai, C.-C. Wang, Y.-H. Chen, R. Vittal, J.-J. Lin, and K.-C. Ho, "A high performance dye-sensitized solar cell with a novel nanocomposite film of

ptnp/mwcnt on the counter electrode," *Journal of Materials Chemistry*, vol. 20, no. 20, pp. 4067–4073, 2010.

[23] X. Zheng, J. Deng, N. Wang, D. Deng, W.-H. Zhang, X. Bao, and C. Li, "Podlike n-doped carbon nanotubes encapsulating feni alloy nanoparticles: High-performance counter electrode materials for dye-sensitized solar cells," *Angewandte Chemie International Edition*, vol. 53, no. 27, pp. 7023–7027, 2014.

[24] Y. Xiao, J. Wu, J.-Y. Lin, S.-Y. Tai, and G. Yue, "Pulse electrodeposition of cos on mwcnt/ti as a high performance counter electrode for a pt-free dye-sensitized solar cell," *Journal of Materials Chemistry A*, vol. 1, no. 4, pp. 1289–1295, 2013.

[25] J.-Y. Lin, J.-H. Liao, and T.-Y. Hung, "A composite counter electrode of cos/mwcnt with high electrocatalytic activity for dye-sensitized solar cells," *Electrochemistry Communications*, vol. 13, no. 9, pp. 977–980, 2011.

[26] G. Yue, J. Wu, J.-Y. Lin, Y. Xiao, S.-Y. Tai, J. Lin, M. Huang, and Z. Lan, "A counter electrode of multi-wall carbon nanotubes decorated with tungsten sulfide used in dye-sensitized solar cells," *Carbon*, vol. 55, pp. 1–9, 2013.

[27] Y. Xing, X. Zheng, Y. Wu, M. Li, W.-H. Zhang, and C. Li, "Nitrogen-doped carbon nanotubes with metal nanoparticles as counter electrode materials for dye-sensitized solar cells," *Chemical Communications*, vol. 51, no. 38, pp. 8146–8149, 2015.

[28] Y. Shi, K. K. Kim, A. Reina, M. Hofmann, L.-J. Li, and J. Kong, "Work function engineering of graphene electrode via chemical doping," *ACS nano*, vol. 4, no. 5, pp. 2689–2694, 2010.

[29] M. Rameez, K. Saranya, A. Subramania, N. Sivasankar, and S. Mallick, "Bimetal (ni–co) nanoparticles-incorporated electrospun carbon nanofibers as an alternative counter electrode for dye-sensitized solar cells," *Applied Physics A*, vol. 122, no. 2, p. 71, 2016.

[30] L. Chen, Y. Zhou, H. Dai, T. Yu, J. Liu, and Z. Zou, "One-step growth of coni 2 s 4 nanoribbons on carbon fibers as platinum-free counter electrodes for fiber-shaped dye-sensitized solar cells with high performance: polymorph-dependent conversion efficiency," *Nano Energy*, vol. 11, pp. 697–703, 2015.

[31] G. Yue, G. Yang, F. Li, and J. Wu, "Pedot: Pss assisted preparation of a graphene/nickel cobalt oxide hybrid counter electrode to serve in efficient dye-sensitized solar cells," *RSC Advances*, vol. 5, no. 121, pp. 100159–100168, 2015.

[32] F. Du, X. Zuo, Q. Yang, B. Yang, G. Li, H. Tang, H. Zhang, M. Wu, and Y. Ma, "The stabilization of nico 2 o 4 nanobelts used for catalyzing triiodides in dye-sensitized solar cells by the presence of rgo sheets," *Solar Energy Materials and Solar Cells*, vol. 149, pp. 9–14, 2016.

[33] S. Y. Khoo, J. Miao, H. B. Yang, Z. He, K. C. Leong, B. Liu, and T. T. Y. Tan, "One-step hydrothermal tailoring of nico2s4 nanostructures on conducting oxide substrates as an efficient counter electrode in dye-sensitized solar cells," *Advanced Materials Interfaces*, vol. 2, no. 18, 2015.

[34] J. Liu, C. Li, Y. Zhao, A. Wei, and Z. Liu, "Synthesis of nico 2 s 4 nanowire arrays through ion exchange reaction and their application in pt-free counter-electrode," *Materials Letters*, vol. 166, pp. 154–157, 2016.

[35] H. Kamisaka, T. Adachi, and K. Yamashita, "Theoretical study of the structure and optical properties of carbon-doped rutile and anatase titanium oxides," *The Journal of chemical physics*, vol. 123, no. 8, p. 084704, 2005.

[36] W. Choi, A. Termin, and M. R. Hoffmann, "The role of metal ion dopants in quantum-sized tio2: correlation between photoreactivity and charge carrier recombination dynamics," *The Journal of Physical Chemistry*, vol. 98, no. 51, pp. 13669–13679, 1994.

[37] H. Wang and J. Lewis, "Second-generation photocatalytic materials: anion-doped tio2," *Journal of Physics: Condensed Matter*, vol. 18, no. 2, p. 421, 2005.

[38] J. Pascual, J. Camassel, and H. Mathieu, "Fine structure in the intrinsic absorption edge of ti o 2," *Physical Review B*, vol. 18, no. 10, p. 5606, 1978.

[39] M. Barberio, P. Barone, V. Pingitore, and A. Bonanno, "Optical properties of tio 2 anatase–carbon nanotubes composites studied by cathodoluminescence spectroscopy," *Superlattices and Microstructures*, vol. 51, no. 1, pp. 177–183, 2012.

[40] P. Barone, M. Barberio, A. Oliva, and A. Bonanno, "Synthesis and characterization of carbon nanotubes wrapped on anatase microparticles," *Particle & Particle Systems Characterization*, vol. 28, no. 3-4, pp. 64–70, 2011.

[41] U. Mehmood, I. A. Hussein, A. Al-Ahmed, and S. Ahmed, "Enhancing power conversion efficiency of dye-sensitized solar cell using tio 2-mwcnt composite photoanodes," *IEEE Journal of Photovoltaics*, vol. 6, no. 2, pp. 486–490, 2016.

[42] M. Kaneko, "I. okura in photocatalysis (eds.: M. kaneko, i. okura), kohdansha," 2002.

[43] M. Barberio, P. Barone, A. Imbrogno, F. Xu, V. Pingitore, and A. Bonanno, "Optical and structural properties of carbon nanotubenrutile heterostructures," *Journal of Chemistry and Chemical Engineering*, vol. 6, no. 10, p. 942, 2012.

[44] S. Ito, T. N. Murakami, P. Comte, P. Liska, C. Grätzel, M. K. Nazeeruddin, and M. Grätzel, "Fabrication of thin film dye sensitized solar cells with solar to electric power conversion efficiency over 10%," *Thin solid films*, vol. 516, no. 14, pp. 4613–4619, 2008.

[45] M. Barberio, P. Barone, A. Imbrogno, A. Bonanno, and F. Xu, "Optical and morphological properties of carbon nanotube—anatase nanocomposites: Improvements in visible absorbance," *Open Journal of Composite Materials*, vol. 4, no. 01, p. 78, 2014.

[46] S. Satapathi, H. S. Gill, S. Das, L. Li, L. Samuelson, M. J. Green, and J. Kumar, "Performance enhancement of dye-sensitized solar cells by incorporating graphene sheets of various sizes," *Applied Surface Science*, vol. 314, pp. 638–641, 2014.

[47] G. Sharma, D. Daphnomili, K. Gupta, T. Gayathri, S. Singh, P. Angaridis, T. Kitsopoulos, D. Tasis, and A. Coutsolelos, "Enhancement of power conversion efficiency of dye-sensitized solar cells by co-sensitization of zinc-porphyrin and thiocyanate-free ruthenium (ii)-terpyridine dyes and graphene modified tio 2 photoanode," *Rsc Advances*, vol. 3, no. 44, pp. 22412–22420, 2013.

[48] N. Yang, J. Zhai, D. Wang, Y. Chen, and L. Jiang, "Two-dimensional graphene bridges enhanced photoinduced charge transport in dye-sensitized solar cells," *ACS nano*, vol. 4, no. 2, pp. 887–894, 2010.

[49] T.-H. Tsai, S.-C. Chiou, and S.-M. Chen, "Enhancement of dye-sensitized solar cells by using graphene-tio2 composites as photoelectrochemical working electrode," *Int. J. Electrochem. Sci*, vol. 6, no. 8, pp. 3333–3343, 2011.

[50] M. Zhu, X. Li, W. Liu, and Y. Cui, "An investigation on the photoelectrochemical properties of dye-sensitized solar cells based on graphene–tio 2 composite photoanodes," *Journal of Power Sources*, vol. 262, pp. 349–355, 2014.

[51] L. Liu, B. Zeng, Q. Meng, Z. Zhang, J. Li, X. Zhang, P. Yang, and H. Wang, "Titanium dioxide/graphene anode for enhanced charge-transfer in dye-sensitized solar cell," *Synthetic Metals*, vol. 222, pp. 219–223, 2016.

[52] T. H. Chowdhury, A. Islam, A. Mahmud Hasan, M. Terdi, M. Arunaku-mari, S. Prakash Singh, M. Alam, I. M. Bedja, M. Hafidz Ruslan, K. Sopian, *et al.*, "Prospects of graphene as a potential carrier-transport material in third-generation solar cells," *The Chemical Record*, vol. 16, no. 2, pp. 614–632, 2016.

[53] P. Lonardo, D. Lucca, and L. De Chiffre, "Emerging trends in surface metrology," *CIRP Annals-Manufacturing Technology*, vol. 51, no. 2, pp. 701–723, 2002.

[54] R. Howland, L. Benatar, and P. S. Instruments, *A practical guide to scanning probe microscopy*. Park scientific instruments, 1996.

[55] P. Eaton and P. West, *Atomic force microscopy*. Oxford University Press, 2010.

[56] B. Corporation, *NanoScope Software* 8.10 *User Guide*. Bruker, 2011.

[57] B. Ferrario, *Introduzione alla tecnologia del vuoto*. Pàtron, 1999.

[58] M. Anderle and M. G. Cattania, *Metodi per la caratterizzazione chimico-fisica delle superfici*. AIV; IRST; Istituto trentino di cultura, 1990.

[59] D. Briggs and J. Grant, "Surface analysis by auger and x-ray photo-electron spectroscopy in im publications and surfacespectra limited," *Chichester/Manchester UK*, 2003.

[60] S. GmbH, *XR50 X-ray source manual*. Specs, 2002.

[61] W. West, "Absorption of electromagnetic radiation," *AccessScience,© McGraw-Hill Companies*, 2008.

[62] T. Ma, X. Fang, M. Akiyama, K. Inoue, H. Noma, and E. Abe, "Properties of several types of novel counter electrodes for dye-sensitized solar cells," *Journal of Electroanalytical Chemistry*, vol. 574, no. 1, pp. 77–83, 2004.

[63] X. Chen, Q. Tang, B. He, L. Lin, and L. Yu, "Platinum-free binary co-ni alloy counter electrodes for efficient dye-sensitized solar cells," *Angewandte Chemie International Edition*, vol. 53, no. 40, pp. 10799–10803, 2014.

[64] J. Zhang, H. Wang, and A. K. Dalai, "Effects of metal content on activity and stability of ni-co bimetallic catalysts for co 2 reforming of ch 4," *Applied Catalysis A: General*, vol. 339, no. 2, pp. 121–129, 2008.

[65] K. Takanabe, K. Nagaoka, K. Nariai, and K.-i. Aika, "Titania-supported cobalt and nickel bimetallic catalysts for carbon dioxide reforming of methane," *Journal of Catalysis*, vol. 232, no. 2, pp. 268–275, 2005.

[66] T. Young, "An essay on the cohesion of fluids," *Philosophical Transactions of the Royal Society of London*, vol. 95, pp. 65–87, 1805.

[67] M. Scarselli, L. Camilli, P. Castrucci, F. Nanni, S. Del Gobbo, E. Gautron, S. Lefrant, and M. De Crescenzi, "In situ formation of noble metal nanoparticles on multiwalled carbon nanotubes and its implication in metal–nanotube interactions," *Carbon*, vol. 50, no. 3, pp. 875–884, 2012.

[68] M. Barberio, F. Stranges, and F. Xu, "Coating geometry of ag, ti, co, ni, and al nanoparticles on carbon nanotubes," *Applied Surface Science*, vol. 334, pp. 174–179, 2015.

[69] N. McIntyre and M. Cook, "X-ray photoelectron studies on some oxides and hydroxides of cobalt, nickel, and copper," *Analytical chemistry*, vol. 47, no. 13, pp. 2208–2213, 1975.

[70] M. C. Biesinger, B. P. Payne, A. P. Grosvenor, L. W. Lau, A. R. Gerson, and R. S. C. Smart, "Resolving surface chemical states in xps analysis of first row transition metals, oxides and hydroxides: Cr, mn, fe, co and ni," *Applied Surface Science*, vol. 257, no. 7, pp. 2717–2730, 2011.

[71] M. Hassel and H.-J. Freund, "High resolution xps study of a thin coo (111) film grown on co (0001)," *Surface Science Spectra*, vol. 4, no. 3, pp. 273–278, 1996.

[72] H. Wang, W. Wei, and Y. H. Hu, "Nio as an efficient counter electrode catalyst for dye-sensitized solar cells," *Topics in Catalysis*, vol. 57, no. 6-9, pp. 607–611, 2014.

[73] S. Gutmann, M. Wolak, M. Conrad, M. Beerbom, and R. Schlaf, "Effect of ultraviolet and x-ray radiation on the work function of tio 2 surfaces," *Journal of Applied Physics*, vol. 107, no. 10, p. 103705, 2010.

[74] M. Shiraishi and M. Ata, "Work function of carbon nanotubes," *Carbon*, vol. 39, no. 12, pp. 1913–1917, 2001.

[75] P. Liu, Q. Sun, F. Zhu, K. Liu, K. Jiang, L. Liu, Q. Li, and S. Fan, "Measuring the work function of carbon nanotubes with thermionic method," *Nano Letters*, vol. 8, no. 2, pp. 647–651, 2008.

[76] A. Andersson, N. Johansson, P. Broms, N. Yu, D. Lupo, W. R. Salaneck, *et al.*, "Fluorine tin oxide as an alternative to indium tin oxide in polymer leds," *Advanced Materials*, vol. 10, no. 11, pp. 859–863, 1998.

[77] D. Deng, L. Yu, X. Chen, G. Wang, L. Jin, X. Pan, J. Deng, G. Sun, and X. Bao, "Iron encapsulated within pod-like carbon nanotubes for oxygen reduction reaction," *Angewandte Chemie International Edition*, vol. 52, no. 1, pp. 371–375, 2013.

[78] J. Zhang, C. Yu, L. Wang, Y. Li, Y. Ren, and K. Shum, "Energy barrier at the n719-dye/cssni3 interface for photogenerated holes in dye-sensitized solar cells," *Scientific reports*, vol. 4, 2014.

[79] M. Cariello, S. Ahn, K.-W. Park, S.-K. Chang, J. Hong, and G. Cooke, "An investigation of the role increasing π-conjugation has on the efficiency of dye-sensitized solar cells fabricated from ferrocene-based dyes," *RSC Advances*, vol. 6, no. 11, pp. 9132–9138, 2016.

[80] S. Suhaimi, M. M. Shahimin, Z. Alahmed, J. Chyskỳ, and A. Reshak, "Materials for enhanced dye-sensitized solar cell performance: Electrochemical application," *Int. J. Electrochem. Sci*, vol. 10, no. 4, pp. 2859–2871, 2015.

[81] D. Zhang, X. Li, S. Chen, F. Tao, Z. Sun, X. Yin, and S. Huang, "Fabrication of double-walled carbon nanotube counter electrodes for dye-sensitized solar sells," *Journal of Solid State Electrochemistry*, vol. 14, no. 9, pp. 1541–1546, 2010.

[82] S. Ni, Z. Li, and J. Yang, "Oxygen molecule dissociation on carbon nanostructures with different types of nitrogen doping," *Nanoscale*, vol. 4, no. 4, pp. 1184–1189, 2012.

[83] C.-Y. Yen, Y.-F. Lin, S.-H. Liao, C.-C. Weng, C.-C. Huang, Y.-H. Hsiao, C.-C. M. Ma, M.-C. Chang, H. Shao, M.-C. Tsai, *et al.*, "Preparation and properties of a carbon nanotube-based nanocomposite photoanode for dye-sensitized solar cells," *Nanotechnology*, vol. 19, no. 37, p. 375305, 2008.

[84] U. Mehmood, I. A. Hussein, K. Harrabi, M. Mekki, S. Ahmed, and N. Tabet, "Hybrid tio 2–multiwall carbon nanotube (mwcnts) photoanodes for efficient dye sensitized solar cells (dsscs)," *Solar Energy Materials and Solar Cells*, vol. 140, pp. 174–179, 2015.

[85] L. Qi, Z. Yin, S. Zhang, Q. Ouyang, C. Li, and Y. Chen, "The increased interface charge transfer in dye-sensitized solar cells based on well-ordered tio 2 nanotube arrays with different lengths," *Journal of Materials Research*, vol. 29, no. 6, pp. 745–752, 2014.

[86] J. Sun, L. Gao, and Q. Zhang, "Synthesizing and comparing the photocatalytic properties of high surface area rutile and anatase titania nanoparticles," *Journal of the American Ceramic Society*, vol. 86, no. 10, pp. 1677–1682, 2003.

[87] A. Mayabadi, V. Waman, M. Kamble, S. Ghosh, B. Gabhale, S. Rondiya, A. Rokade, S. Khadtare, V. Sathe, H. Pathan, *et al.*, "Evolution of structural and optical properties of rutile tio 2 thin films synthesized

at room temperature by chemical bath deposition method," *Journal of Physics and Chemistry of Solids*, vol. 75, no. 2, pp. 182–187, 2014.

[88] M. Barberio, A. Imbrogno, D. R. Grosso, A. Bonanno, and F. Xu, "Study of dye absorption in carbon nanotube-titanium dioxide heterostructures," *J. Chem*, vol. 9, pp. 245–252, 2015.

[89] M. Amirnasr, M. K. Nazeeruddin, and M. Grätzel, "Thermal stability of cis-dithiocyanato (2, 2′-bipyridyl4, 4′ dicarboxylate) ruthenium (ii) photosensitizer in the free form and on nanocrystalline tio 2 films," *Thermochimica Acta*, vol. 348, no. 1, pp. 105–114, 2000.

[90] U. Mehmood, K. Harrabi, I. A. Hussein, and S. Ahmed, "Enhanced photovoltaic performance of dye-sensitized solar cells using tio 2-graphene microplatelets hybrid photoanode," *IEEE Journal of Photovoltaics*, vol. 6, no. 1, pp. 196–201, 2016.

[91] H. Cai, J. Li, X. Xu, H. Tang, J. Luo, K. Binnemans, J. Fransaer, and D. E. De Vos, "Nanostructured composites of one-dimensional tio 2 and reduced graphene oxide for efficient dye-sensitized solar cells," *Journal of Alloys and Compounds*, vol. 697, pp. 132–137, 2017.